High precision many-electron calculations for multiply-charged ions

seit 1558

Dissertation
To Fulfill the Requirements for the Degree of
doctor rerum naturalium (Dr. rer. nat.)

Submitted to the Council of the Faculty of Physics and Astronomy
of the Friedrich Schiller University Jena

by M.Phil. **Moazzam Bilal**

born on 20.08.1981 in Gujranwala, Pakistan

Gutachter

1. Prof. Dr. Stephan Fritzsche,
   Helmholtz-Institut Jena, Deutschland
   Friedrich-Schiller-Universität Jena, Germany
2. Prof. Dr. Andrey Surzhykov,
   Physikalisch-Technische Bundesanstalt, Germany
   Technische Universität Braunschweig, Germany
3. Priv.-Doz. Dr. Zoltán Harman
   Max Planck Institute for Nuclear Physics
   Saupfercheckweg 1, 69117 Heidelberg, Germany

Date of defense: 29.10.2019

Abstract

Recent advances in measurements/observations have made it possible to test small and minute fundamental physical effects for transition rates and line strengths in many-electron atomic systems with unprecedented accuracies. This thesis provides high-precision calculations of line strengths and lifetimes for different atomic systems where we accurately account for various higher-order effects. In all these systems, systematically enlarged multiconfiguration Dirac-Hartree-Fock (MCDHF) wave functions are employed for calculation of the atomic states involved in the transitions to account for the relativistic correlation corrections.

Firstly, the QED sensitive magnetic dipole ($M1$) line strengths between the fine-structure levels of the ground configurations in B-, F-, Al- and Cl-like ions are calculated for the four elements argon, iron, molybdenum and tungsten. For these transitions, in addition to relativistic correlation corrections, the QED corrections are evaluated to all orders in αZ utilizing an effective potential approach. As a result, our calculations have reached an accuracy of 10^{-4} for the $M1$ line strengths. These accurate theoretical predictions provide the prerequisite for a test of QED by lifetime measurements at different frequencies and timescales. This will help to find a reason for the present discrepancies between theory and experiment for B-like Ar and Al-like Fe.

Secondly, the line strength of the $1s^2 2s2p\ ^1P_1$ – $1s^2 2s^2\ ^1S_0$ spin allowed $E1$ transition in Be-like carbon is calculated. For this highly correlated transition, different correlation models are developed to account for all major electron-electron correlation contributions. The finite nuclear mass effect is accurately calculated taking into account the energy, wave functions as well as operator contributions. As a result, a reliable theoretical benchmark of $E1$ line strength with a relative accuracy of 1.5×10^{-4} is provided to support high precision lifetime measurement at GSI Darmstadt for the $1s^2 2s2p\ ^1P_1$ state in Be-like carbon.

Finally, large-scale calculations are performed for all allowed ($E1$) and forbidden ($M1, E2, M2$) transitions among the fine structure levels of the $3s^2 3p^5$, $3s3p^6$ and $3s^2 3p^4 3d$ configurations for Ni XII. Here, we validate all recently identified tentative experimental lines with one exception. Moreover, we present *ab initio* lifetimes that are better than previously reported *ab initio* and semi-empirical values as compared to available experimental data. Thus, we provide reliable predictions in the prospects of future experiments.

Zusammenfassung

Jüngste Fortschritte bei Messungen/Beobachtungen ermöglichen es, kleine und sehr kleine physikalische Effekte auf Übergangsraten und Linienstärken atomarer Mehrelektronensysteme mit nie dagewesener Genauigkeit zu testen. Diese Dissertation beinhaltet hochpräzise Berechnungen von Linienstärken und Lebensdauern für verschiedene atomare Systeme unter akkurater Berücksichtigung verschiedener Effekte höherer Ordnung. Bei allen diesen Systemen werden systematisch vergrößerte Multikonfigurations-Dirac-Hartree-Fock-Wellenfunktionen (MCDHF-Wellenfunktionen) verwendet, um relativistische Korrelationskorrekturen in die Berechnung der an den Übergängen beteiligten atomaren Zustände miteinzubeziehen.

Zuerst werden die QED-empfindlichen Linienstärken der magnetischen Dipolübergänge ($M1$-Übergänge) zwischen den Feinstrukturniveaus der Grundkonfigurationen von B-, F-, Al- und Cl-ähnlichen Ionen der vier Elemente Argon, Eisen, Molybdän und Wolfram berechnet. Zusätzlich zu relativistischen Korrelationskorrekturen werden für diese Übergänge die QED-Korrekturen mittels eines effektiven Potentials in allen Ordnungen in αZ ausgewertet. Daraus resultiert eine Genauigkeit von 10^{-4} für die von uns berechneten $M1$-Linienstärken. Diese akkuraten theoretischen Vorhersagen stellen die Voraussetzung für einen Test der QED durch Messungen von Lebensdauern bei verschiedenen Frequenzen und auf verschiedenen Zeitskalen dar. Dies wird dazu beitragen, einen Grund für die gegenwärtigen Diskrepanzen zwischen Theorie und Experiment im Bezug auf B-ähnliches Ar und Al-ähnliches Fe zu finden.

Zweitens wird die Linienstärke des spin-erlaubten $1s^2 2s2p\ ^1P_1 - 1s^2 2s^2\ ^1S_0$ $E1$-Übergangs in Be-ähnlichem Kohlenstoff berechnet. Für diesen hochkorrelierten Übergang werden verschiedene Korrelationsmodelle entwickelt um die Beiträge aller wichtigen Elektron-Elektron-Korrelationen zu berücksichtigen. Der Effekt der endlichen Kernmasse wird präzise berechnet, unter Einbeziehung der Beiträge zu Energien, Wellenfunktionen und Operatoren. Daraus resultiert ein verlässlicher theoretischer Maßstab für die $E1$-Linienstärke mit einer relativen Genauigkeit von 1.5×10^{-4} zur Unterstützung hochgenauer Messungen der Lebensdauer des $1s^2 2s2p\ ^1P_1$-Zustands in Be-ähnlichem Kohlenstoff an der GSI Darmstadt.

Zuletzt werden umfangreiche Berechnungen für alle erlaubten ($E1$) und verbotenen ($M1$, $E2$, $M2$) Übergänge zwischen den Feinstrukturniveaus der $3s^2 3p^5$-, $3s3p^6$- und $3s^2 3p^4 3d$-Konfigurationen in Ni XII durchgeführt. Hier bestätigen wir alle kürzlich identifizierten vorläufigen experimentellen Linien mit einer Ausnahme. Darüber hinaus präsentieren wir *Ab-initio*-Lebensdauern, die besser mit den verfügbaren experimentellen Daten übereinstimmen als bisherige *Ab-initio*- und semiempirische Werte, und stellen so verlässliche Vorhersagen für zukünftige Experimente bereit.

Contents

1 Introduction

Our understanding of the structure and dynamics of many-electron atoms and ions depends on a detailed analysis and comparison of theoretical predictions with experimental observations of atomic properties. Two important and complementary properties of atomic states are transition energies and transition rates. For transition energies, the present experimental accuracy reaches the order of $10^{-6} - 10^{-18}$ [1–3]. Here the interplay between experiment and theory has improved drastically our understanding of different (higher-order) effects, e.g., many-body relativistic, the Breit interaction, finite nuclear mass, and quantum electrodynamics (QED) effects [4, 5]. Moreover, this interplay has a great potential in the search for new physics [6] and it eventually leads towards testing the Standard Model. For example, QED has been tested at the level of 7.2% for the magnetic dipole ($M1$) transition energy between fine-structure levels of the ground configuration in B-like Ar [7–10].

It is equally desirable to test the Standard Model by high precision atomic lifetime (the inverse of the sum of all transition rates of a given atomic state) measurements [11]. For the transition rates and line strengths, in contrast, the accuracy level is often not yet sufficient to test QED, many-body relativistic effects, etc. This is partially due to theory and partially due to experiment. From theory: we know that transition rates depend on a higher power of transition energy and non-diagonal matrix elements i.e., line strengths of the multi-polar electromagnetic operators. In contrast to the calculation of transition energies, there is no variational principle available that defines a minimum condition for the optimization of non-diagonal matrix elements. For this reason, the many-body relativistic effects (and/or higher-order effects) are more difficult to capture. From experiments: most if not all the measurements/observations provide uncertainties in the region of $30 - 1\%$ mainly due to systematic and statistical errors [11, 12].

For $M1$ transitions, however, there are two remarkable exceptions where accuracy in the order of 0.1% is claimed by efficiently controlling the systematic and statistical errors. These lifetime measurements were performed at the Heidelberg electron beam ion trap (HD-EBIT). The measured lifetime is reported as 9.573(4)(5)(stat/syst) ms for the $2s^2 2p\ ^2P_{3/2}$ level in B-like Ar [13] and 16.726(+20/-10) ms for the $3s^2 3p\ ^2P_{3/2}$ level in Al-like Fe [14]. These levels decay via an $M1$

transition to the ground states $2s^2 2p\ ^2P_{1/2}$ and $3s^2 3p\ ^2P_{1/2}$, respectively.

The line strengths for these $M1$ transitions, in the non-relativistic limit, are insensitive to the description of the many-electron wave functions. In other words, (almost) all correlation corrections are of relativistic origin and, therefore, suppressed by a factor αZ, where Z is the nuclear charge. These line strengths are especially sensitive to QED contributions. For instance, the leading QED effect of an order α, so-called electron anomalous magnetic moment (EAMM) correction, contributes to 0.46% [15]. Therefore, such $M1$ transition line strengths can be calculated very precisely and may be used as a benchmark for comparison with the experiment. However, the most precise theoretical evaluations for these line strengths in B-like ions [15–20] and in Al-like ions [21, 22] predict shorter lifetimes than measured experimentally [13, 14]. In fact, the deviation between theory and experiment is of the order of the EAMM, which led to speculation about the correctness of the inclusion of the EAMM into the transition amplitude. Let us note here that such high-precision measurements are available only from the HD-EBIT in the millisecond range. In the future, however, precise experiments for various lifetime and transition energy domains and by different techniques will hopefully solve the present discrepancy. Therefore, there is a strong need for a theoretical analysis of these systems where relativistic correlations and the QED contributions can be quantified as a benchmark principal for these experiments.

For the $E1$ strong transition, high hopes are pinned on the femtosecond laser technology [23], which has already demonstrated great success in studies of chemical reactions, wave function dynamics, photoionization time delays, etc. This technology allows to perform the highly accurate pump-probe atomic lifetime measurements. The pump-probe technique has been used already in the lifetime measurements of the $6P_{3/2}$ excited-state in cesium atom which is relevant to the atomic parity non-conservation [24, 25]. In contrast to neutral atoms, transitions to exited states in ions quickly reach the XUV- or X-ray energy range and, therefore, a high-photon flux of XUV- or X-ray source is required for pumping and/or probing processes. For instance, the Linac Coherent Light Source has been employed in the measurement of lifetimes in Ne-like iron [26]. Recently, it has been proposed to use a compact high-power XUV-ray source in a combination with the storage ring at GSI to perform precision spectroscopy and lifetime measurements of ions [27]. For this purpose, a novel high-photon flux XUV-radiation source based on the high harmonic generation in argon has been developed, which provides ∼100 femtosecond pulses at photon energies up to 26.6 eV [28, 29]. As the first experiment, the measurement of the lifetime of the $1s^22s2p\ ^1P_1$ state in Be-like carbon is proposed with a relative accuracy in the order of $10^{-4} - 10^{-5}$ [27].

The excited state $1s^22s2p\ ^1P_1$ decays to the $1s^22s^2\ ^1S_0$ ground state through a strong spin allowed $E1$ transition. For the line strength of this transition, theoretical testing of higher-order physics is a formidable task. Be-like carbon is low charge state ion and this transition is within the same shell ($\Delta n = 0$). Here the biggest challenge is to control uncertainties due to electron-electron correlations. During past years, various theoretical studies have been reported for this line strength [30–36]. As a result, the most accurate theoretical calculations [32, 35, 36] report an accuracy in the order of 10^{-3}. Since the expected experimental accuracy is much better, there is a need for further improvements in the theoretical calculations.

The other important realm of the interplay between theory and observation is diagnostic of astrophysical and laboratory plasmas. The astrophysical and plasma physics communities require new and increasingly accurate theoretical predictions for the identification and interpretation of the high-resolution spectroscopic observations of ionized atoms in all ionization stages. In addition to the quality, the quantity of spectra of these stripped ions is also needed for the determination of plasma parameters, such as electron temperature, electron density, elemental abundances, etc [37].

Chlorine like nickel (Ni XII) is an important member in the group of iron-peak elements. Such nickel ions exist in different astronomical objects [38–42]. Indeed, nickel has been found the second most abundant transition element in our sun after iron. Extreme ultraviolet (EUV) and soft x-rays from Ni XII are prominent in solar emission lines and also in solar-type stars [43–45]. Moreover, Edlen and Smitt have observed several forbidden coronal lines in the visible and UV region of the solar spectrum from such ions [46]. Similarly, nickel is also an important impurity element in the Joint European Torus (JET) (from both divertor and limiter configurations) [47] as well as in many other tokamak fusion test reactor plasmas [48–50]. Several EUV emission lines from Ni XII have also been observed in beam-foil experiment in laboratory plasma [51, 52].

Despite the importance of Ni XII ions, only a few of the level energies are well characterized in the literature [53]. This is mainly because the experimental data can only be compared with less predictive *ab initio* or even semi-empirical calculations. Very recently, Del Zanna and Badnell suggested several new experimental excitation energies for Ni XII based on different observations [54] and semi-empirical term energy correction method [55, 56]. They then used their semi-empirical data combined with experimental data for the determination of the transition rates and electron impact excitation rates for Ni XII [54]. The semi-empirical formalism is often advantageous, this, however may contain a source of ambiguity because these predictions are not fully according to atomic structure theory [11, 57]. The reliability of this formalism can be improved by either more experimental data are available in advance for the theoretical adjustments or by the comparison with accurate *ab initio* calculations.

In this thesis, we focus on three regimes of high-precision calculations for transition rates in many-electron atomic systems in the view of continuous experimental/observational advances as mentioned above. The thesis is structured in the following way:

We start with Chapter 2 where we explain the generation of approximate relativistic wave functions for many-electron atomic systems within the framework of the multi-configuration Dirac-Hartree-Fock method (MCDHF) method. These approximate wave functions are improved by systematically enlarging the configuration space to include the correlation effects. Further improvements are implemented by including Breit, first order QED and finite nuclear mass corrections. Then these wave functions are used to calculate the transition amplitudes necessary for the calculation of transition properties of different multi-pole expansions of the electromagnetic field.

In Chapter 3, we present a detailed study for the line strengths of QED-sensitive $M1$ forbidden transitions between the fine-structure levels of the ground configurations in B-, Al-, F- and Cl-like ions. The ground configurations of B-like and Al-like ions have a valence p-electron in the L shell and M shell, respectively. These configurations are also quite similar to the ground configurations of F-like and Cl- like ions but with a p-shell vacancy in the L shell and M shell, respectively. The major difference between the two systems of ions is the flip of fine-structure levels where the excited ^2P levels dominantly decay through $M1$ transition to the ground-state ^2P levels. We predict lifetimes in the millisecond to picoseconds range with a relative accuracy of 10^{-4} by means of our accurate line strengths

Chapter 4 deals with a detailed calculation of $E1$ line strength of the $1s^22s2p\ ^1P_1 -\ 1s^22s^2\ ^1S_0$ transition in Be-like carbon. Contrary to $M1$ transition, this transition is highly correlated. Here, we develop various electron correlation models and use orthogonal and nonorthogonal set of orbitals for the initial and final states in these correlation models. We find that the accuracy assessment, based on an agreement between the gauges, might lead to a significant error underestimation. For this reason, we estimate the uncertainty from the differences between the results obtained within all the correlation models developed. Finally, we analyse the effect of the finite nuclear mass to the line strength and demonstrate its gauge invariance as we take the recoil correction to the transition operator into account. We obtain a calculated line strength of 2.43926(37) with a relative accuracy of 1.5×10^{-4}.

In Chapter 5, we perform intensive computation to improve the database for transition rates, oscillator strengths, and lifetimes on Ni XII, an important astrophysical ion. Thereby, we take into account all allowed $E1$ and forbidden $M1$, $E2$, and $M2$ transitions among the first 31 lowest energy levels. These lines arise from three configurations $3s^23p^5$, $3s3p^6$ and $3s^23p^43d$. We present the same level of accuracy or even better than the semi-empirical calculations. We testify recent tentative identification for the observed lines, and then predict the atomic data for the lines which have not been observed yet.

Finally, the results of this thesis are summarized in Chapter 6.

The atomic units ($\hbar = 1$, $e = 1$, $m_e = 1, c = 1/\alpha$) are used throughout the work unless stated otherwise.

2 Many-electron wave functions

The laws of nature should be expressed in beautiful equations.

Paul M. Dirac (1902 – 1984)

2.1 Dirac-Coulomb Hamiltonian

Like in one electron systems, the first step for the calculations of atomic stationary states and transitions among them for atoms or ions with N electrons is writing down the Hamiltonian $\hat{H}$ to be used in solving the wave equation (eigenvalue problem)

$$\hat{H}\Psi = E\Psi\,. \tag{2.1}$$

for the complete atomic wave function Ψ [58]. Here the Hamiltonian $\hat{H}$ is the sum of N one-electron contributions $\hat{H}(i)$ and $N(N-1)/2$ two-electron contributions $\hat{H}(ij)$ so that

$$\hat{H} = \sum_{i=1}^{N} \hat{H}(i) + \sum_{i<j}^{N} \hat{H}(ij)\,. \tag{2.2}$$

For the relativistic calculations of the atomic stationary states, the dominant relativistic corrections are considered by accounting for the motion of each electron according to Dirac theory for the one-electron operator and by considering only the instantaneous Coulomb interaction for the two-electron operator [59, 60]. The resulting Hamiltonian is the so-called Dirac-Coulomb Hamiltonian given as

$$\begin{aligned} \hat{H}_{\mathrm{DC}} &= \sum_{i=1}^{N} \hat{h}_{\mathrm{D}}(i) + \sum_{i<j}^{N} \frac{1}{r_{ij}} \\ &= \sum_{i=1}^{N} \left[c\boldsymbol{\alpha}_i \cdot \boldsymbol{p}_i + (\beta_i - 1)c^2 + V_{\mathrm{nuc}}(r_i) \right] + \sum_{i<j}^{N} \frac{1}{r_{ij}}\,, \end{aligned} \tag{2.3}$$

where $\hat{h}_{\mathrm{D}}$ is the one electron Dirac Hamiltonian, c is the speed of light, $V_{\mathrm{nuc}}(r_i)$ is usually considered as an effective electron-nucleus potential at radius r_i by taking into account the finite size of the nuclear charge distribution through a two parameter Fermi distribution of the charge, $\boldsymbol{p} \equiv -i\boldsymbol{\nabla}$ the electron momentum operator and

$r_{ij} = |\boldsymbol{r}_i - \boldsymbol{r}_j|$ is the distance between electrons i and j. The $\boldsymbol{\alpha}$ and β are 4×4 Dirac matrices given by

$$\alpha_i = \begin{pmatrix} 0 & \sigma_i \\ \sigma_i & 0 \end{pmatrix}, \quad \beta = \begin{pmatrix} I & 0 \\ 0 & -I \end{pmatrix}. \tag{2.4}$$

in terms of the 2×2 Pauli matrices σ_i and zero and unit matrix I. Explicitly, in $\hat{H}_{\mathrm{DC}}$ (2.3) the one electron terms describe the kinetic and potential energy of the each electron with respect to nucleus, and the two electron terms the Coulomb potential energy between any two electrons.

2.2 Central field approximations

The two electrons terms in the Hamiltonian (2.3) are problematic in that they destroy the separability of the Hamiltonian and introduce singularities into the wave equation when $r_{ij} = 0$. These electron-electron interactions make the exact solution of the Eq. (2.1) almost impossible. One possibility to get the insight into the nature of the wave function is to apply such physical approximations to the Hamiltonian (2.3) so that the Eq. (2.1) is solvable. One such approximation is central-field approximation which has proved quite successful. According to this approximation $\hat{H}_{\mathrm{DC}}$ can be written as

$$\hat{H}_o = \sum_{i=1}^{N} \left[c\boldsymbol{\alpha}_i \cdot \boldsymbol{p}_i + (\beta_i - 1)c^2 + V_{\mathrm{nuc}}(r_i) + u_i(r_i) \right], \tag{2.5}$$

where $u_i(r_i)$ depends only on r and not on the angular coordinates. In this approximation each electron is assumed to move in a spherically symmetric, electrostatic potential which is independent of the other electrons but is the time-averaged field of the $N - 1$ electrons. We can define a central field as $V_i^C(r) = V_{\mathrm{nuc}}(r) + u_i(r)$ of spherical symmetry for each electron. This leads to the so-called independent particle model where many-electron wave functions can be expressed as a simple product of one electron solutions of the Eq. (2.5).

The approximate Hamiltonian $\hat{H}_o$ commutes with $\hat{H}_{\mathrm{DC}}$ as well as with total angular momentum operators $\boldsymbol{J}^2$ and J_z. We may choose the eigenfunction of $\hat{H}_o$

which are also eigenfunctions of these operators. Similar to Eq. (2.1) we can write,

$$\hat{H}_o \Psi_o = E_o \Psi_o \,. \tag{2.6}$$

As mentioned above, $\hat{H}_o$ is separable we can write,

$$E_o = \sum_{i=1}^{N} E_i \,, \tag{2.7}$$

and

$$\Psi_o = \prod_{i=1}^{N} \phi_{a_i}(\boldsymbol{r}_i) \,. \tag{2.8}$$

where a represents all of the quantum numbers and $\phi_{a_i}(\boldsymbol{r})$ are Dirac orbitals which are the solution of the Dirac equation

$$\Big[c\boldsymbol{\alpha} \cdot \boldsymbol{p} + (\beta - 1)c^2 + V^C(r) \Big] \phi(a; \boldsymbol{r}) = E \phi_a(\boldsymbol{r}) \,. \tag{2.9}$$

The individual Dirac orbital has the following four-spinor form in a spherical coordinate system of (r, θ, φ),

$$\phi_{n\kappa m}(\boldsymbol{r}) = \frac{1}{r} \begin{pmatrix} P_{n\kappa}(r)\, \chi_{\kappa m}(\theta, \varphi) \\ iQ_{n\kappa}(r)\, \chi_{-\kappa m}(\theta, \varphi) \end{pmatrix}, \quad \text{with} \quad \langle \phi_a | \phi_b \rangle = \delta_{ab} \,. \tag{2.10}$$

In this four-spinor expression, n is the principal quantum number of bound electrons, κ is the relativistic quantum number, which has $\kappa = \pm(j + \frac{1}{2})$ for $j = l \mp \frac{1}{2}$, and m is the projection of the total angular momentum j on the quantization axis. In the expression (2.10), $P_{n\kappa}(r)$ and $Q_{n\kappa}(r)$ denote the large and small components of the electron radial wave functions. The two-component function $\chi_{\kappa m}(\theta, \varphi)$ is referred to as the spin-angular function and is defined by [61],

$$\chi_{\kappa m}(\theta, \varphi) = \sum_{m_s = \pm 1/2} \langle l, m - m_s; 1/2, m_s | jm \rangle \, Y_{l, m-m_s}(\theta, \varphi) \, \xi_{m_s} \,, \tag{2.11}$$

where $\langle l, m - m_s; 1/2, m_s | jm \rangle$ denotes a Clebsch-Gordan coefficient, $Y_{l,m-m_s}(\theta, \varphi)$ is a spherical harmonic, and

$$\xi_{+1/2} = \begin{pmatrix} 1 \\ 0 \end{pmatrix}, \quad \xi_{-1/2} = \begin{pmatrix} 0 \\ 1 \end{pmatrix}. \tag{2.12}$$

2.3 Configuration state function

In the non-relativistic case, one approach to obtain the approximate wave function (2.8) is Hartree approximation. This approximation, however, does not give the antisymmetric wave function since the electrons are indistinguishable fermions and Pauli exclusion principle is not satisfied. Pauli exclusion principle can be satisfied by taking an approximate wave function in the form of a Slater determinant:

$$\Psi_o = \frac{1}{\sqrt{N!}} \begin{vmatrix} \phi_{a_1}(\boldsymbol{r_1}) & \phi_{a_1}(\boldsymbol{r_2}) & \cdots & \phi_{a_1}(\boldsymbol{r_N}) \\ \phi_{a_2}(\boldsymbol{r_1}) & \phi_{a_2}(\boldsymbol{r_2}) & \cdots & \phi_{a_2}(\boldsymbol{r_N}) \\ \vdots & \vdots & \vdots & \vdots \\ \phi_{a_N}(\boldsymbol{r_1}) & \phi_{a_N}(\boldsymbol{r_2}) & \cdots & \phi_{a_N}(\boldsymbol{r_N}) \end{vmatrix} . \tag{2.13}$$

Here, $N!$ is the factorial of N. The approximate wave functions in the form of Slater determinant, however, are not eigenfunctions of total angular momentum operator. Since the aim is to construct the basis functions which give the approximate wave functions as close as possible to accurate wave functions; the basis are taken in the form of configuration state functions (CSFs).

A CSF, represented as $\Phi(\gamma;\pi JM)$, is formed by taking linear combination of Slater determinants (2.13) constructed from the orbitals (2.10) so as to obtain normalized ($\langle\Phi(\gamma;\pi JM)|\Phi(\gamma;\pi JM)\rangle = 1$) eigenfunctions of the total angular momentum operators $\boldsymbol{J}^2$ and J_z, and parity π. The label γ represents the electron configuration and all information such as orbital occupation numbers, coupling, seniority numbers, etc., required to define the CSF uniquely. The Slater determinants in a CSF belong to same electronic configuration, i.e. with same n and l quantum numbers but with different m quantum numbers. This process is known as coupling and the CSFs are also referred coupled basis functions.

In our discussion so far, we have shown how the exact wave function can be approximated as a single CSF ($\Psi = \Phi(\gamma;\pi JM)$) which is constructed by taking the radial wave functions of the approximations (2.5) and angular coupling between the orbitals. Now we want to improve the accuracy of the approximate wave function by determining the set of radial wave functions that will provide the best estimate. One such way is to apply the variational method to optimize the total energy so that the energy functional is stationary with respect to variation in the radial wave functions which leads to so-called Dirac-Hartree-Fock (DHF) equations. This approximation is called DHF approximation and the approximate wave functions are called DHF wave functions. The derivations and solution method of these equations can be considered as a special case of the approximations that we will discuss in the next section.

The DHF method predicts many atomic properties remarkably well, however, for the high precision calculations these are considered insufficient. As this is independent particle method, where the electrons are assumed to move in an average, central field of the other electrons and the nucleus, so the notion of 'correlation in the motion of the electrons (electron-electron correlations)' is entirely neglected.

2.4 Multi-configuration Dirac-Hartree-Fock method

To effectively evaluate the electron-electron correlation effects, here we use the multiconfiguration Dirac-Hartree-Fock (MCDHF) method in jj-coupling [59, 60]. In this method, the wave function Ψ of an atomic state label Γ, total angular momentum quantum number J, magnetic quantum number M and parity π is referred to as an atomic state function (ASF) which is represented as $\Psi(\Gamma;\pi JM)$. In contrast to DHF method, in MCDHF method the ASF is expanded in the basis of, say n_c CSFs of the same symmetry:

$$\Psi(\Gamma;\pi JM) = \sum_{j=1}^{n_c} C_j^\Gamma \Phi(\gamma_j;\pi JM), \quad \text{where} \quad \sum_{j=1}^{n_c} |C_j^\Gamma|^2 = 1\,. \tag{2.14}$$

Here C_j^Γ are the expansion coefficients or weights which represent the atomic state Γ in the basis of CSFs. The expansion coefficients may be combined in column vector $\boldsymbol{C}^\Gamma \equiv \{C_j^\Gamma, j = 1, \ldots, n_c\}$. In single CSF case (DHF), only the radial functions are varied. However, in MCDHF approach there are two phases of optimization need to be performed simultaneously on the basis of Dirac-Coulomb Hamiltonian (2.3):

- the determination of C_j^Γ coefficients for a given set of CSFs. This process is called relativistic configuration interaction (RCI) process and
- optimization of the radial wave functions that define the orbitals for the construction of basis of CSFs for a given set of C_j^Γ coefficients.

Now we explain in some details about the variational formalism for the optimization processes mentioned above. Basically, the variational method for solving the Eq. (2.1) relies on the reformulation of the eigenvalue problem. For the normalized wave function $\Psi(\Gamma; \pi JM)$ the total energy is the expectation value of the Hamiltonian $\hat{H}_{\mathrm{DC}}$ (2.3), referred to as energy functional,

$$E[\Psi] = \langle \Psi | \hat{H}_{\mathrm{DC}} | \Psi \rangle \,, \quad \text{with the condition} \quad \langle \Psi | \Psi \rangle = 1 \,. \tag{2.15}$$

It is obvious that the definition of $\Psi(\Gamma; \pi JM_J)$ includes the radial functions and expansion coefficients. These are varied to get the best estimate Ψ^{best} which leaves the energy functional stationary ($\delta E = 0$) with respect to variations $\delta\Psi$ so that $\delta\Psi$ is orthogonal to Ψ with the boundary conditions, namely

$$\langle \delta\Psi | \hat{H}_{\mathrm{DC}} - E | \Psi^{\text{best}} \rangle = 0 \,. \tag{2.16}$$

The orthogonality constraints must also be included in the variational process. As a result, the allowed variations of the radial functions are of two types: those that involve only a single radial function and those that require that two radial functions be perturbed simultaneously in order to maintain orthonormality.

We explain in some more details about the derivations and solution method for the MCDHF equations. Let $a, b, c, \ldots$ represent one-electron radial functions for an orthonormal set of Dirac orbitals (2.10) with associated quantum numbers $n_a\kappa_a, n_b\kappa_b, n_c\kappa_c, \ldots$. The resulting energy functional is written in the form

$$\mathcal{F}(\{c\}, \{P\}, \{Q\}; \gamma J) = \langle \Psi | \hat{H}_{\mathrm{DC}} | \Psi \rangle + \sum_{ab} \delta_{\kappa_a \kappa_b} \lambda_{ab} \mathcal{C}_{ab} \,. \tag{2.17}$$

In this expression, the Lagrange multipliers λ_{ab} for orbitals a and b belonging to same κ space ($\kappa_a = \kappa_b$) are introduced to constrain the variations in the one-electron functions ($\delta P_{n\kappa}, \delta Q_{n\kappa}$), namely

$$\mathcal{C}_{ab} \equiv \int \left[P_a(r) P_b(r) + Q_a(r) Q_b(r) \right] dr - \delta_{n_a n_b} = 0 \,. \tag{2.18}$$

which guarantees the orthonormality of the one-electron functions as well as of the CSFs.

The energy (2.15) associated to an ASF (Γ) can be represented in the matrix form as,

$$\begin{aligned}
E_{\mathrm{DC}}^{(\Gamma;\pi JM)} &= \langle\Psi(\Gamma;\pi JM)|\hat{H}_{\mathrm{DC}}|\Psi(\Gamma;\pi JM)\rangle \\
&= \sum_{i,j} C_i^{\Gamma *} C_j^{\Gamma} \langle\Phi(\gamma_i;\pi J)|\hat{H}_{\mathrm{DC}}|\Phi(\gamma_j;\pi J)\rangle \\
&= \sum_{i,j} C_i^{\Gamma *} C_j^{\Gamma} H_{ij}^{(\Gamma;\pi J)} \,. \qquad (2.19)
\end{aligned}$$

where $\mathbf{H}^{(\Gamma;\pi\mathrm{J})}$ is matrix of dimension $n_c \times n_c$ with elements $H_{ij}^{(\Gamma;\pi J)}$. The Hamiltonian $\hat{H}_{\mathrm{DC}}$ is invariant under spatial rotation and reflections therefore the elements $H_{ij}^{(\Gamma;\pi J)}$ are independent of the projection quantum number M. We can skip projection quantum number M in the definition of CSF for the energy expression. The predicted atomic energy levels $E^{(\Gamma;\pi JM)}$ can be taken to be the eigenvalues of $\mathbf{H}^{(\Gamma;\pi\mathrm{J})}$ and C_i^{Γ} are components of associated eigenvectors. Therefore, the construction of the matrix $\mathbf{H}^{(\Gamma;\pi\mathrm{J})}$ with respect to the basis of CSFs plays a central role in RCI and MCDHF calculations.

Traditionally, the matrix $\mathbf{H}^{(\Gamma;\pi\mathrm{J})}$ among the basis of CSFs can be expressed in terms of spin angular coefficients and radial integrals

$$\langle\Psi|\hat{H}_{\mathrm{DC}}|\Psi\rangle = \sum_{ab} t_{ab} I(a,b) + \sum_{abcd;k} v_{abcd}^{k} R^{k}(ab,cd) \,. \qquad (2.20)$$

In this expansion,

$$t_{ab} = \sum_{ij} t_{ab}^{ij} C_i^{\Gamma} C_j^{\Gamma} \,, \quad v_{abcd;k} = \sum_{ij} v_{abcd;k}^{ij} C_i^{\Gamma} C_j^{\Gamma} \,, \qquad (2.21)$$

are the angular coefficients (scalar) which arise from integrating over the angular degrees of freedom and depend on the angular coupling scheme of the CSFs i and j and on orbital angular momenta j_a, j_b, j_c, j_d. The expressions $I(a,b)$ and $R^k(ab,cd)$ are one-electron and two-electron relativistic integrals over radial amplitudes, respectively, given as

$$
\begin{aligned}
I(a,b) &= \langle a|h_D|b\rangle \\
&= \delta_{\kappa_a\kappa_b}\int_0^\infty \{P_a(r)V_{\mathrm{nuc}}(r)P_b(r) \\
&\quad -cP_a(r)\left(\frac{d}{dr}-\frac{\kappa_a}{r}\right)Q_b(r) \\
&\quad +cQ_a(r)\left(\frac{d}{dr}+\frac{\kappa_a}{r}\right)P_b(r) \\
&\quad +Q_a(r)(V_{\mathrm{nuc}}(r)-2c^2)Q_b(r)\}dr\,,
\end{aligned}
\tag{2.22}
$$

which contains the kinetic and potential energy of an electron in a subshell, and

$$
R^k(ab,cd)=\int_0^\infty [P_{n_a\kappa_a}(r)P_{n_c\kappa_c}(r)+Q_{n_a\kappa_a}(r)Q_{n_c\kappa_c}(r)]\frac{1}{r}Y^k(bd;r)dr\,, \tag{2.23}
$$

describe the effective interaction strength of the four electrons involved in the interaction [62]. In this expression the Y^k functions are defined as

$$
Y^k(ab;r)=r\int_0^\infty \frac{r_<^k}{r_>^{k+1}}[P_{n_a\kappa_a}(s)P_{n_b\kappa_b}(s)+Q_{n_a\kappa_a}(s)Q_{n_b\kappa_b}(s)]ds\,. \tag{2.24}
$$

Here $r_>$ ($r_<$) denotes the greater (lesser) of r and s.

In RCI problem, the CSFs are assumed to be known by taking some initial estimate of the radial functions $\{P_{n\kappa},Q_{n\kappa}\}$ and only the expansion coefficients $\boldsymbol{C}^\Gamma \equiv \{C_j^\Gamma, j=1,\ldots,n_c\}$ are optimized by demanding that the functional (2.17) be stationary with respect to variation in coefficients leading to eigenvalue problem for the expansion coefficients,

$$
(\mathbf{H}^{(\Gamma;\pi J)}-E_{\mathrm{DC}}^{(\Gamma;\pi J)}\mathbf{1})\boldsymbol{C}^\Gamma=0\,. \tag{2.25}
$$

Here $\mathbf{1}$ is $n_c\times n_c$ unit matrix. This equations has many solutions. Only one eigenvector is desired eigenvector, not necessarily the lowest one, and this vector defines the expansion coefficients.

Finally, for a given set of expansion coefficients $\boldsymbol{C}^\Gamma$, the stationary condition with respect to the variations in both large and small component of the radial functions result in coupled MCDHF equations:

$$w_a \begin{bmatrix} V(a;r) & -c\left[\frac{d}{dr} - \frac{\kappa_a}{r}\right] \\ c\left[\frac{d}{dr} - \frac{\kappa_a}{r}\right] & V(a;r) - 2c^2 \end{bmatrix} \begin{bmatrix} P_a(r) \\ Q_a(r) \end{bmatrix} = \sum_b \varepsilon_{ab} \delta_{\kappa_a \kappa_b} \begin{bmatrix} P_a(r) \\ Q_a(r) \end{bmatrix}, \tag{2.26}$$

where $V(a;r) = (V_{\text{nuc}}(r) + Y(a;r) + \bar{X}(a;r))$. In this expression $Y(a;r)$ is direct potential and $\bar{X}(a;r)$ contains the exchange contributions arising form both diagonal and off-diagonal matrix elements appearing in expression (2.19). In each κ-space, Lagrange related energy parameters ε_{ab} are introduced to impose the orthonormality constraint (2.18) in the variational process.

Taking an initial estimate of the radial functions, solutions to MCDHF equations are obtained by an iterative process which is referred to as self-consistent field (SCF) method. Very efficient methods are used to solve the differential equations by using finite difference methods where the radial functions are represented on a logarithmic mesh. Essentially, in every iteration, the method improves the radial functions.

As explained earlier, the equations for the expansion coefficients and the radial functions are coupled, the RCI problem and the SCF process are iterated until the radial orbitals and the energies are converged to a specific tolerance.

For the construction of the variational functional, we have a choice of combining expressions for the energies of one or more ASFs. Moreover, ASFs can be included in the calculations to have different total angular momenta. If the functionals are weighted sums of energies of all possible ASFs that may be constructed from a given set of CSFs then these are called average level (AL) calculations. In this case, the number of ASFs is same as the number, n_c , of CSFs in the set. If the configuration included in the calculation have differing total angular momenta, then the extension of the AL method is called extended average level (EAL) [63].

If a variational functional is constructed to minimize the energy for only one ASF then this scheme is called the optimal level (OL) scheme. Whereas in the extended optimal level (EOL) scheme the calculations can be extended to include several ASFs. In this case the ASFs which are subset of the total ASFs that can be generated from a given set of configurations. In EOL case, the energy functional contains the weights only for the levels under consideration [63]. In this thesis, we have employed OL and EOL schemes for the optimization of atomic states. This gives us freedom to choose simultaneous or separate optimization of the orbitals for the desired ASFs. We will explain the details of atomic systems and relevant atomic states in the later Chapters.

For the implementation of MCDHF/RCI methods, the credit goes to two main developments in the form of computer programs [61, 63]. However, the application and scope of the problem were limited due to available computer resources and numerical algorithms to solve the equations. Almost a decade later from these developements, there was a tremendous improvement in this regard in the form of *General-purpose Relativistic Atomic Structure Program* (GRASP)[64] which is an assembly of different codes. And then there were many modifications and extensions to the GRASP to increase the accuracy of the atomic properties by improving the computational capabilities to increase the size of the wave functions [65–67]. The widely used latest versions are GRASP2K [68] and its descendant in Fortran 95 with name GRASP2018 [69]. In the work presented in this thesis, we have employed the latest version GRASP2K [68] to generate energy levels and wave functions of atomic states of many-electron atoms and ions for the calculations of necessary transition properties.

The latest version GRASP2K can generate the wave functions comprising of millions of CSFs. However, it is not possible to optimize all radial orbitals belonging to these wave functions simultaneously. Instead, the calculations are done layer by layer in a procedure of active set approach. We explain this procedure in the next section.

2.5 Active set approach

For many atomic properties, if the electron-electron interactions are considered in full extent even for a small number of electrons (say, $N = 4$), the computations become a formidable task. The basis sets are infinite, but in practice, the basis set must be restricted to a finite subset making the choice of basis and subset an important factor that most of the time depends on the property and the system under study. Some systems are highly correlated (e.g., near neutral atomic systems particularly for $E1$ transitions) and other are less correlated (e.g. $M1$ transitions between the fine structure states belonging to the same configuration). We shall describe this correlation business in detail for different systems and related correlations effects in the later Chapters.

Briefly, in all those atomic systems we have incorporated important electron correlations using systematically enlarged many-electron wave functions i.e., the configuration space is systematically extended using the active set approach and monitoring the numerical convergence of the desired parameters. In the active set approach, the electrons are virtually excited from reference configurations to a set of orbitals called the active set. The calculations are started for the lowest order of approximations where the orbitals belonging to the so-called reference configurations are optimized spectroscopically, i.e., the orbitals are required to have a node structure similar to corresponding hydrogenic orbitals. These orbitals are named as spectroscopic orbitals. After the initial calculations, the wave functions are systematically improved by performing MCDHF calculations for each new layer of orbitals and keeping the previously calculated orbitals fixed. These added orbitals are called correlation orbitals. For each new layer of correlation orbitals the basis of CSFs is expanded by including further single (S), single and double (SD), single, double and triple (SDT) and some times single, double, triple and quadruple (SDTQ) virtual excitations from the configurations defining the reference set to the active set of orbitals [67].

2.6 Higher-order corrections

For high precision calculations of the many-electrons systems, one needs to go beyond the instantaneous Coulomb interaction for the two-electron operator defined in Dirac-Coulomb Hamiltonian (2.3).

2.6.1 Breit correction

The leading corrections to instantaneous Coulomb interaction, such as magnetic interaction and the effects of retardation, are implemented using assumption based on one-electron concepts [70]. Taking the approximation of the order α^2 from QED, one can derive the so-called transverse photon interaction Hamiltonian which is given as

$$\begin{aligned}\hat{H}_{\mathrm{TP}} &= -\sum_{i<j}^{N}\Bigg[\boldsymbol{\alpha}_i\cdot\boldsymbol{\alpha}_j\frac{\cos(\omega_{ij}r_{ij}/c)}{r_{ij}}\\ &+ (\boldsymbol{\alpha}_i\cdot\boldsymbol{\nabla}_i)(\boldsymbol{\alpha}_j\cdot\boldsymbol{\nabla}_j)\frac{\cos(\omega_{ij}r_{ij}/c)-1}{\omega_{ij}^2 r_{ij}/c^2}\Bigg]\,. \end{aligned} \tag{2.27}$$

In this expression, given in Coulomb gauge, ω_{ij} represents the energy of the virtual exchanged photon between two electrons introduced in QED, even in the absence of the emission or absorption of 'real' radiation. The value of ω_{ij} can be interpreted in terms of differences in orbital one-electron energies. This may be an appropriate assumption for singly occupied orbitals but is not correct for multiply occupied ones and certainly is not true for correlation orbitals. For these reasons transverse photon interaction is often computed in the low-frequency limit ($\omega_{ij} \to 0$), the expression (2.27) reduces to frequency independent Breit interaction (that most of the time is called the Breit interaction) given as

$$\hat{H}_{\mathrm{Breit}} = -\sum_{i<j}^{N}\frac{1}{2r_{ij}}\left[\boldsymbol{\alpha}_i\cdot\boldsymbol{\alpha}_j + \frac{(\boldsymbol{\alpha}_i\cdot\boldsymbol{r}_{ij})(\boldsymbol{\alpha}_j\cdot\boldsymbol{r}_{ij})}{r_{ij}^2}\right]. \tag{2.28}$$

Adding (2.28) to the Dirac-Coulomb Hamiltonian (2.3) gives the Dirac-Coulomb-Breit Hamiltonian (in the effective Coulomb gauge)

$$\hat{H}_{\mathrm{DCB}} = \hat{H}_{\mathrm{DC}} + \hat{H}_{\mathrm{Breit}}\,. \tag{2.29}$$

2.6.2 QED corrections

The leading quantum electrodynamic (QED) corrections; the self-energy (SE) correction and the vacuum polarization (VP) can be added to $\hat{H}_{\mathrm{DCB}}$ to yield the updated Hamiltonian

$$\hat{H}_{\mathrm{DCB+QED}} = \hat{H}_{\mathrm{DCB}} + \hat{H}_{\mathrm{SE}} + \hat{H}_{\mathrm{VP}}\,. \tag{2.30}$$

Here $\hat{H}_{\mathrm{SE}}$ provides the SE correction. This correction arises from the interaction of the electron with its own radiation field. This correction is applied to diagonal energies as

$$\langle \Phi(\gamma_i;\pi J)|\hat{H}_{\mathrm{SE}}|\Phi(\gamma_i;\pi J)\rangle = \sum_{a=1}^{n_w} w_a E_{\mathrm{SE}(a)}\,, \tag{2.31}$$

where n_w is the number of subshells in the CSF, n_a is the number of electrons in subshell a in the CSF, $E_{SE}(a)$ is the one-electron self-energy of an electron in subshell a. In GRASP2K [68] the self-energy correction is computed from a screened-hydrogenic approximation, a model that does not apply well to correlation orbitals that are far from hydrogenic approximations. It is better to specify the largest principal quantum number for which CSFs are to be considered in the self-energy correction. For small calculations with a few correlation orbitals this cut-off is set to the largest principal quantum number of the included orbitals. In large calculations with many correlation orbitals the cut-off is typically set to a number which is just one/two number larger than the highest principal quantum number of the spectroscopic orbitals.

In the expression (2.30), $\hat{H}_{\mathrm{VP}}$ provides the correction due to vacuum polarization, which is related to the creation and annihilation of virtual electron–positron pairs in the field of the nucleus. This correction is applied to all matrix elements

$$\langle \Phi(\gamma_i;\pi J)|\hat{H}_{\mathrm{VP}}|\Phi(\gamma_j;\pi J)\rangle = \langle \Phi(\gamma_i;\pi J)|\sum_{i}^{N} V_{\mathrm{Uehl}}(r)|\Phi(\gamma_j;\pi J)\rangle\,, \tag{2.32}$$

where $V_{\mathrm{Uehl}}(r)$ is Uehling potential which describe correction to the nuclear Coulomb potential. It includes vacuum polarization potential terms of both second- and fourth-order in QED perturbation theory [60].

2.6.3 Nuclear recoil correction

The correction due to the finite nuclear mass is much more difficult to consider. In non-relativistic theory, the center-of-mass motion can be separated off exactly. For one-electron ions, this simply leads to using a reduced mass for the electron, for many-electron atoms mass polarization terms arise which are the origin of the Hughes-Eckart shifts [71]. The full relativistic theory of the nuclear recoil effect can be formulated only within quantum electrodynamics [72]. However, the lowest order relativistic nuclear recoil correction can be applied to get the leading order nuclear recoil correction [73].

The lowest order nuclear motional corrections, namely the normal mass shift (NMS) term based on Dirac kinetic energy operator

$$\hat{H}_{\mathrm{NMS}} = \frac{1}{M}\sum_{i=1}^{N}\Big[c\boldsymbol{\alpha}_i \cdot \boldsymbol{p}_i + (\beta_i - 1)c^2\Big], \tag{2.33}$$

where M is the nuclear mass, and mass polarization term named as the specific mass shift (SMS)

$$\hat{H}_{\mathrm{SMS}} = \frac{1}{M}\sum_{i<j=1}^{N}\boldsymbol{p}_i \cdot \boldsymbol{p}_j, \tag{2.34}$$

are added to the Dirac-Coulomb Hamiltonian (2.3).

Breit, QED and nuclear recoil corrections are computed using the MCDHF orbitals from a calculation using the Dirac-Coulomb Hamiltonian (2.3) and then applying only the RCI method with a Hamiltonian that includes the desired corrections. Generally, the most important correction is the Breit correction with the Dirac-Coulomb-Breit Hamiltonian (2.28) [60].

In the following section, we will briefly explain how the obtained wave functions are further utilized to calculate the many-electron transition properties.

2.7 Many-electron transition amplitudes

After each layer of MCDHF and subsequently RCI calculations, transition properties, such as transition rates A, line strengths S, and weighted oscillator strengths gf from atomic state Γ_i to atomic state Γ_j are computed in terms of reduced matrix elements:

$$\langle\Psi(\Gamma_i;\pi_i J_i)||\boldsymbol{T}^{\mathrm{EMK}}||\Psi(\Gamma_j;\pi_j J_j)\rangle\,, \tag{2.35}$$

where the operator $\boldsymbol{T}^{\mathrm{EMK}}$ depends on the multipolarity, $E1, M1, E2, M2$, etc., of the transition. Inserting the CSF expansions for the atomic states, the reduced matrix element are expressed as sum over reduced matrix elements between CSFs

$$\begin{aligned}&\langle\Psi(\Gamma_i;\pi_i J_i)||\boldsymbol{T}^{\mathrm{EMK}}||\Psi(\Gamma_j;\pi_j J_j)\rangle\\ =&\sum_{i,j} C_i^{\Gamma *} C_j^{\Gamma}\langle\Phi(\gamma_i;\pi_i J_i)||\boldsymbol{T}^{\mathrm{EMK}}||\Phi(\gamma_j;\pi_j J_j)\rangle\end{aligned} \tag{2.36}$$

Using Racah algebra techniques, these matrix elements between the CSFs are finally obtained as sums over radial integrals

$$\langle\Phi(\gamma_i;\pi_i J_i)||\boldsymbol{T}^{\mathrm{EMK}}||\Phi(\gamma_j;\pi_j J_j)\rangle=\sum_{a,b} d_{ab}(i,j)\langle n_a\kappa_a||\boldsymbol{T}^{\mathrm{EMK}}||n_b\kappa_b\rangle \tag{2.37}$$

where the d_{ab} are derived from the angular coefficients (2.21) described above. The above procedure assumes that the two atomic states Γ_i and Γ_j are built from the same set of optimized orbitals. When the orbitals are separately optimized for both states, the evaluation of this matrix element becomes very time consuming since the non-orthogonalities of the initial and final state orbital sets prevent Racah algebra to be used. For this case, the representation of the two states are changed in such a way that orbital sets become biorthonormal [74]. For the two states expanded in CSFs

$$\sum_i C^{\Gamma_i}\Phi(\gamma_i;\pi_i J_i) \quad \text{and} \quad \sum_j C^{\Gamma_j}\Phi(\gamma_j;\pi_j J_j)\,, \tag{2.38}$$

the orbital sets $\{\phi_i\}\rightarrow\{\phi'_i\}$ and $\{\phi_j\}\rightarrow\{\phi'_j\}$ are transformed to a biorthonormal basis, i.e. $\langle\phi'_i|\phi'_j\rangle=\delta_{ij}$. The orbital transformation in effect changes the CSFs, and we have

$$\Phi(\gamma_i;\pi_i J_i)\rightarrow\Phi'(\gamma_i;\pi_i J_i) \quad \text{and} \quad \Phi(\gamma_j;\pi_j J_j)\rightarrow\Phi'(\gamma_j;\pi_j J_j)\,. \tag{2.39}$$

The orbital transformation is followed by a counter-transformation of the expansion coefficients $\{C^{\Gamma_i}\}\rightarrow\{C'^{\Gamma_i}\}$ and $\{C^{\Gamma_j}\}\rightarrow\{C'^{\Gamma_j}\}$ so as to leave the wave functions invariant, i.e.

$$\sum_i C^{\Gamma_i}\Phi(\gamma_i;\pi_i J_i)\equiv\sum_i C'^{\Gamma_i}\Phi'(\gamma_i;\pi_i J_i)\,,$$

and

$$\sum_j C^{\Gamma_j}\Phi(\gamma_j;\pi_j J_j)\equiv\sum_j C'^{\Gamma_j}\Phi'(\gamma_j;\pi_j J_j)\,. \tag{2.40}$$

In the new representation standard Racah algebra can be used to evaluated transition matrix elements.

It is important to note that for the transition amplitude, the corrections which are mentioned in this Chapter improve only the wave functions and the energies related to the states involved in the transition. However, for high precision calculations, sometimes we need to consider these corrections to the transition operator involved in the transition as well. We will explain in Chapter 3 in details that the QED correction to the transition operator has a significant effect on $M1$ transition. Similarly, in Chapter 4, we will demonstrate that nuclear recoil correction should also be considered to $E1$ transition operator for accurate transition rate calculation.

3 $M1$ forbidden transition in B-,Al-,F- and Cl-like ions

In this chapter, we shall present high precision calculations for the line strengths of magnetic dipole transitions between the $2s^2 2p\ ^2P_{3/2} - {}^2P_{1/2}$ levels in B-like, the $3s^2 3p$ $^2P_{3/2} - {}^2P_{1/2}$ levels in Al-like, the $2s^2 2p^5\ ^2P_{1/2} - {}^2P_{3/2}$ levels in F-like and the $3s^2 3p^5$ $^2P_{1/2} - {}^2P_{3/2}$ levels in Cl-like ions for the four elements argon, iron, molybdenum and tungsten [75]. These line strengths can be calculated very precisely because in non-relativistic theory these are independent of the wave function description. The calculated lifetimes of the respective upper states from these transition will lie in the millisecond to picoseconds range and may be used as a benchmark for comparison with the experiments.

This Chapter is structured in the following way: a short description of the $M1$ line strength in the non-relativistic limit is described in Sec. 3.1. In this section, we also describe how total line strength is obtained by adding higher-order corrections to non-relativistic line strength. Evaluation of the relativistic correlation corrections to the line strength is presented in Sec. 3.2. In Sec. 3.3, we evaluate the QED corrections to all orders in αZ. In Sec. 3.4, we present a detailed comparison of our calculated line strengths with other theories. Furthermore, adding the contributions from $E2$ channel for these transitions, we predict the lifetimes of the excited states of the ground configurations in B-, Al-, F- and Cl-like ions and compare with available experiments.

3.1 Theory - Basic formulas

The magnetic dipole transition probability from an upper state i to a lower state f is expressed in terms of the line strength as

$$A_{ij}^{M1} = \frac{4}{3} \frac{\omega^3}{c^3} \mu_0^2 \frac{S}{2J_i + 1}, \tag{3.1}$$

where μ_0 denotes the Bohr magneton, c is the speed of light, $\omega = E_i - E_f$ the transition energy and S is the line strength given as

$$S = \frac{18c^4}{\omega^2} \left|\langle \Psi_f \parallel \mathbf{T}^{M1} \parallel \Psi_i \rangle\right|^2 . \tag{3.2}$$

$\mathbf{T}^{M1}$ is the $M1$ transition operator given as

$$\mathbf{T}^{M1} = \frac{1}{\sqrt{2}}\, j_1(\omega r/c)\, \frac{[\boldsymbol{\alpha} \times \mathbf{r}]}{r} \;=\; \frac{\sqrt{2}}{r} j_1(\omega r/c)\boldsymbol{\mu} . \tag{3.3}$$

Here $\boldsymbol{\mu} = -[\mathbf{r} \times \boldsymbol{\alpha}]/2$ is relativistic magnetic moment operator, $\boldsymbol{\alpha}$ is Dirac matrix and j_1 is the spherical Bessel function.

In the non-relativistic limit the expansion of $j_1(\omega r/c)$ can be restricted to the first term, and this gives rise to the more familiar $M1$ transition operator

$$\mathbf{T}^{M1}_{\mathrm{nr}} \;=\; -\frac{\sqrt{2}}{3}\,\frac{\omega}{c}\mu_0 \, (\boldsymbol{L} + 2\boldsymbol{S}) . \tag{3.4}$$

where $\boldsymbol{L}$ and $\boldsymbol{S}$ are the orbital and spin angular momentum operators, respectively. In the LS-coupling scheme, which is realized in the non-relativistic case, the $M1$ line strength is nonzero only between fine-structure levels with $\Delta J = \pm 1$. The reduced matrix element of $\mathbf{T}^{M1}_{\mathrm{nr}}$ within the LS-coupling is given by

$$\begin{aligned}\langle J_f \parallel \mathbf{T}^{M1}_{\mathrm{nr}} \parallel J_i \rangle &= -\,\frac{\sqrt{2}}{3}\,\frac{\omega}{c}\mu_0 \langle J_f \parallel (\boldsymbol{J} + \boldsymbol{S}) \parallel J_i \rangle \\ &= -\,\frac{\sqrt{2}}{3}\frac{\omega}{c}\mu_0 \langle J_f \parallel \boldsymbol{S} \parallel J_i \rangle ,\end{aligned}$$

which implies,

$$S_{\mathrm{nr}} = \left|\langle J_f \parallel \boldsymbol{S} \parallel J_i \rangle\right|^2 . \tag{3.5}$$

Therefore, in the non-relativistic limit the line strength S_{nr} is completely determined by the quantum numbers of the initial and final states and does not depend on the radial part of the many-electron wave functions of the initial and final states. For the ${}^2P_{1/2} - {}^2P_{3/2}$ and ${}^2P_{3/2} - {}^2P_{1/2}$, fine-structure transitions, the non-relativistic line strength results in the value of 4/3.

The total line strength can be calculated by adding different corrections to the non-relativistic line strength as follows,

$$S = S_{\rm nr} + \Delta S_{\rm D} + \Delta S_{\rm CI,C} + \Delta S_{\rm CI,B} + \Delta S_{\rm QED} + \Delta S_{\rm rec} \,. \tag{3.6}$$

Here $\Delta \mathrm{S}_\mathrm{D}$ is the correction due to the relativistic motion of the electrons as described by the (single-electron) Dirac equation. This corrections is calculated as a difference between line strength evaluated between Eq. (3.5) and Eq. (3.2). In Eq. (3.2) the initial and final state wave functions are linear combination of Slater determinants constructed in terms of one-electron Dirac wave functions which are the solution of the non-interacting one electron Dirac Hamiltonian.

The next two terms in Eq. (3.6) are due to the relativistic electron-electron interaction (correlations). While the first term $\Delta S_{\rm CI,C}$ arises from the Coulomb interaction, and the second $\Delta S_{\rm CI,B}$ occurs due to the Breit interaction. Both of these terms are evaluated in details in Sec. 3.2. The next correction $\Delta S_{\rm QED}$ originates from QED diagrams, namely, the self-energy diagrams. It is calculated here to all orders in αZ. The evaluation of this term is described in Sec. 3.3.

Finally, $\Delta S_{\rm rec}$ is the correction to the line strength due to the finite nuclear mass effect. This effect can be calculated only by using a rigorous QED approach as described by Volotka *et al.* [17]. According to this approach the recoil corrected magnetic moment operator is given by

$$\boldsymbol{\mu} = -\mu_0 \left(\mathbf{L} + 2\mathbf{S} - \frac{1}{M} \sum_{i,j} [\mathbf{r}_i \times \mathbf{p}_j] \right) , \tag{3.7}$$

where M is mass of the nucleus. Hence the correction to the line strength due to the nuclear recoil can be written as

$$\begin{aligned} \Delta S_{\rm rec} &\simeq -2 \langle J_f \parallel (\mathbf{L} + 2\mathbf{S}) \parallel J_i \rangle \\ &\quad \times \langle J_f \parallel \frac{1}{M} \sum_{i,j} [\mathbf{r}_i \times \mathbf{p}_j] \parallel J_i \rangle \,. \end{aligned} \tag{3.8}$$

However, these contributions are very small at the present level of accuracy compared to the leading non-relativistic value 4/3. For example $\Delta S_{\rm rec}$ amounts to 0.000021, 0.000015, 0.000009 and 0.000005 for B-like Ar, Fe, Mo, and W ions, respectively. Therefore, we do not present these values in our final table of the various contribution to line strengths.

3.2 Correlation corrections

In order to evaluate the interelectronic correlation correction arising due to Coulomb interaction $\Delta S_{\mathrm{CI,C}}$, we apply systematically enlarged many-electrons wave functions as described in details in chapter 2. In brief, we started our calculations with the lowest-order of approximation. For this the wave functions for the states with $J = 1/2$ and $J = 3/2$ are calculated within the basis of the multi- reference (MR) configurations. The CSFs in the MR set are generated from the configurations $\{1s^2 2s^2 2p,\ 1s^2 2p^3\}$, $\{1s^2 2s^2 2p^6 3s^2 3p,\ 1s^2 2s^2 2p^6 3p^3\}$, $1s^2 2s^2 2p^5$ and $1s^2 2s^2 2p^6 3s^2 3p^5$ for the B-, Al-, F- and Cl-like ions, respectively. After the initial calculations, the wave functions are systematically improved by performing MCDHF calculations using the active set approach described in Sec. 2.5. Here for each new layer of correlation orbitals the basis of CSFs is expanded by including further SD virtual excitations from the configurations defining the MR set to the active set of orbitals. The active set of orbitals is spanned by the orbitals with a principal quantum number $n \leq 7$ and with azimuthal quantum number $l \leq 6$.

Following each of the MCDHF calculations, separate RCI calculations are performed to further improve the initial and final state wave functions. These allowed us to evaluate the correction due to the Breit interaction $\Delta S_{\mathrm{CI,B}}$ to the line strength. For these calculations the Dirac-Coulomb Breit Hamiltonian (2.28) is used.

The sum of these two corrections gives rise to the total relativistic correlation correction ΔS_{CI}. These contributions are presented in Table 3.1 as a function of the size of the increasing active set labeled by the highest principal quantum number n of the of orbitals considered for the correlations. For the sake of brevity, we present the results only for the Fe ions. As seen from Table 3.1, the convergence with regard to the size of the active set is fairly achieved which allows us to set an absolute uncertainty for the correlation correction to a range 1×10^{-5} to 5×10^{-5} depending on the particular ion.

3.3 QED correction

The QED correction to the $M1$ line strength ΔS_{QED} can be derived in lowest order in αZ by modifying the $M1$ transition operator of the atomic magnetic moment for the EAMM, as discussed in details by Tupitsyn *et al.* [15]. The contribution of the

Table 3.1: Correlation correction ΔS_{CI} to the $M1$ line strength of the transition between the fine-structure levels of the ground configuration for B-, F-, Al- and Cl-like Fe ions. The MCDHF and RCI methods are employed to evaluate these corrections considering Coulomb and Breit type interactions. They are presented as a function of the size of the increasing active set (AS) labeled by the highest principal quantum number n of the orbitals starting from the MR set.

AS	B-like Fe	F-like Fe	Al-like Fe	Cl-like Fe
MR	0.00053	0.00154	0.00149	0.00167
3	0.00052	0.00146	0.00148	0.00165
4	0.00049	0.00151	0.00146	0.00164
5	0.00050	0.00153	0.00145	0.00164
6	0.00045	0.00146	0.00147	0.00165
7	0.00045	0.00145	0.00147	0.00164

EAMM amounts to $\Delta S_{\mathrm{QED,EAMM}} = 0.00618$. Moreover, Volotka *et al.* [16] calculated the one-loop QED correction for several B-like ions to all orders in αZ within the so-called original Furry picture - and by taking into account only the Coulomb potential of the nucleus. We now consider an *extended* Furry picture which includes a local screening potential in the unperturbed Hamiltonian, and extend the calculations for F-, Al-, and Cl-like systems. This extension enables us to account partially for the screening QED corrections by evaluating only one-electron QED diagrams. In the extended Furry picture, we solve the Dirac equation with an effective spherically symmetric potential treating the interaction with the external Coulomb potential of the nucleus and the local screening potential exact to all orders. We employ here the core-Hartree screening potential, which is given by the expression

$$V_{\mathrm{scr}}(r) = \int_0^\infty \mathrm{d}r' \frac{1}{r_>} \rho_{\mathrm{core}}(r') \,. \tag{3.9}$$

Here ρ_{core} denotes the total radial charge density distribution of the core electrons

$$\begin{aligned} \rho_{\mathrm{core}}(r) = \sum_c \left[P_c^2(r) + Q_c^2(r) \right] \,, \\ \int_0^\infty dr \rho_{\mathrm{core}}(r) = n_c \,, \end{aligned} \tag{3.10}$$

where n_c is the number of the core electrons, i.e., n_c = 4, 8, 12, 16 for B-, F-, Al-, and Cl-like ions, respectively. This screening potential is generated self-consistently by solving the Dirac equation until the energies of the core and valence states become

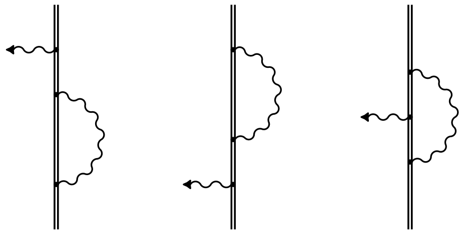

Figure 3.1: Feynman diagrams that represent the self-energy correction to the line strength. The wavy line indicates the photon propagator and the double line indicates the bound-electron wave functions and propagators in the effective potential being the sum of Coulomb and screening potentials. The single photon emission is depicted by the wavy line with arrow.

stable with the relative accuracy of 10^{-9}. To estimate the sensitivity of the result on the choice of the potential several tests have been performed with other screening potentials: Kohn-Sham, Dirac-Hartree, and Dirac-Slater constructed for the initial as well as for the final state. It has been found out, that a relative difference between results obtained with different potentials does not exceed 5×10^{-4}. Overall, therefore, the uncertainty is dominated by a numerical error, which is everywhere smaller than 10^{-5}.

The one-loop QED correction to the line strength consists of the self-energy and vacuum-polarization terms. However, the vacuum-polarization correction previously evaluated in the Uehling approximation appears to be two − four orders of magnitude smaller than the self-energy correction beyond the EAMM approximation [76]. For this reason, we neglect the vacuum-polarization term in the present consideration. The self-energy contribution is given by the diagrams depicted in Fig. 3.1.

While the formulas derived by Volotka *et al.* [16] in the original Furry picture remain formally the same, let us remind that the Dirac spectrum is now generated by solving the Dirac equation with the effective potential. We make use of the implementation of Volotka *et al.* [16] who presented a detailed description of these calculations for B-like ions.

3.4 Results and discussion

Table 3.2 lists different corrections to the non-relativistic line strength for the $M1$ transition between the fine-structure levels of the ground configurations in B-like and F-like Ar, Fe, Mo and W ions. These corrections refer to two different systems of p subshells, one with a single valence electron and other with a single vacancy in the L shell. Table 3.3 shows similar results as Table 3.2 but for the M shell for Al-like and Cl-like Fe, Mo and W ions. As seen from Tables 3.2 and 3.3 the relativistic correction ΔS_{D} is most important.

Its value increases by an order of magnitude for the Mo and W ions when compared to Ar and Fe ions. The correlation correction arising due to Breit interaction turns out to be relatively small as compared to corrections arising due to Coulomb interaction. For Mo and W ions these corrections provide essential contributions to the total line strengths. The next important correction arises from the self-energy (QED). Generally, the lowest order QED correction i.e., the inclusion of EAMM to the transition operator, is considered enough for such type of transitions. As discussed in sections 3.3 this correction amounts to 0.00618 the total line strength. However, the present estimates of the QED correction show that the inclusion of the EAMM is enough only for low Z. For the heavier systems the present rigorous calculations of QED corrections within an extended Furry picture approach are necessary. Finally, all corrections sum to the total line strength S. In order to estimate the total uncertainty we have to note here that the contribution of the negative-energy excitations is not taken into account in present calculations. Since the value of the negative-continuum term strongly depends on an employed one-electron basis functions [15] varying them we estimate its contribution to be less than half of the correlation effect. The uncertainties of individual terms presented in Tables 3.2 and 3.3 as discussed above in corresponding subsections are much smaller than the uncertainty due to the negative-continuum contribution. Therefore, the total uncertainty of the line strength S obtained is fully determined by missing negative-continuum contribution.

In order to compare our results with previous computations, we make use of the line strength from $M1$ transition rates based on Eq. (3.1). We took the same transition energies that have been used in respective calculations. It should be noted that we have added the QED contribution to the line strengths in respective theoretical values wherever this effect has not been considered. For B-like Ar, which

Table 3.2: Individual corrections to the $M1$ non-relativistic line strength $S_{\mathrm{nr}} = 4/3$ for the $(2s^2 2p)\,^2P_{1/2} - {}^2P_{3/2}$ transition in B-like as well as for the $(2s^2 2p^5)\ {}^2P_{3/2} - {}^2P_{1/2}$ transitions in F-like Ar, Fe, Mo and W ions. The total line strength (S) is compared with other theories. The uncertainties involved in the calculation of line strengths are given within the parentheses.

	Ar	Fe	Mo	W
B-like				
ΔS_{D}	-0.00295	-0.00633	-0.01800	-0.07402
$\Delta S_{\mathrm{CI,C}}$	0.00056	0.00038	-0.00247	-0.00530
$\Delta S_{\mathrm{CI,B}}$	0.00001	0.00007	0.00042	0.00166
ΔS_{QED}	0.00617	0.00615	0.00606	0.00567
S	1.33714(28)	1.33362(23)	1.3194(10)	1.2614(18)
	1.3372[1]	1.3337[1]	1.3197[1]	
	1.33693(26)[2]	1.333[3]*		
	1.337[3]*	1.333[4]*		
	1.337[4]*			
F-like				
ΔS_{D}	-0.00295	-0.00633	-0.01800	-0.07402
$\Delta S_{\mathrm{CI,C}}$	0.00094	0.00143	0.00258	0.00569
$\Delta S_{\mathrm{CI,B}}$	0.00000	0.00002	0.00006	0.00036
ΔS_{QED}	0.00617	0.00615	0.00607	0.00568
S	1.33749(47)	1.33460(70)	1.3240(13)	1.2710(30)
	1.356(5)[5]*	1.335[7]*	1.324[8]*	1.271[6] *
	1.338[6]*	1.334[6]*	1.324[6]*	1.271[9]*
		1.3270[10]*	1.3211[10]*	

[1] MCDHF theory by Froese Fischer *et al.* [20].
[2] MC-DFS theory by Tupitsyn *et al.* [15].
[3] MCDF theory by Rynkun *et al.* [18].
[4] MCDF theory by Marques *et al.* [19].
[5] Relativistic coupled-cluster theory by Nandy [77].
[6] MCDF theory by Jönnson *et al.* [78].
[7] MCDF theory by Jonauskas *et al.* [79].
[8] MCDF theory by Aggarwal and Keenan [80].
[9] MCDF theory by Aggarwal and Keenan [81].
[10] Relatively coupled-cluster theory by Nandy and Sahoo [82].
* The original values are corrected by adding the QED correction obtained here.

Table 3.3: Individual corrections to the $M1$ non-relativistic line strength $S_{\rm nr} = 4/3$ for the $(3s^2 3p)\,^2P_{1/2} - \,^2P_{3/2}$ transition in Al-like as well as for the $(3s^2 3p^5)\,^2P_{3/2} - \,^2P_{1/2}$ transition in Cl-like Fe, Mo and W ions. The total line strength (S) is compared with other theories. The uncertainties involved in the calculation of line strengths are given within the parentheses.

	Fe	Mo	W
Al-like			
$\Delta S_{\rm D}$	-0.00302	-0.00950	-0.05025
$\Delta S_{\rm CI,C}$	0.00146	0.00230	0.00340
$\Delta S_{\rm CI,B}$	0.00001	0.00007	0.00054
$\Delta S_{\rm QED}$	0.00617	0.00614	0.00595
S	1.33797(73) 1.336[1]∗ 1.337[2]	1.3324(13)	1.2928(20)
Cl-like			
$\Delta S_{\rm D}$	-0.00302	-0.00950	-0.05025
$\Delta S_{\rm CI,C}$	0.00164	0.00294	0.00615
$\Delta S_{\rm CI,B}$	0.00000	0.00005	0.00029
$\Delta S_{\rm QED}$	0.00617	0.00614	0.00595
S	1.3381(18) 1.338[3]∗ 1.338[5]	1.3330(15)	1.2955(32) 1.295[4]∗ 1.29[6]∗

[1] MR-MP theory by Vilkas and Ishikawa [21].
[2] MR-MP theory by Santana *et al.* [22].
[3] B-spline single-particle orbitals method by Moehs *et al.* [83].
[4] MCDF method by Aggarwal and Keenan [84].
[5] MR-MP theory by Ishikawa *et al.* [85].
[6] MCDF theory by Singh and Puri [86].
* The original values are corrected by adding the QED correction obtained here.

has received much attention over the last decade, our result of total line strength 1.33714(28) corroborates the two exceptionally agreeing calculations from Tupitsyn *et al.* [15] and from Froese Fisher *et al.* [20]. Tupitsyn *et al.* [15] reported the line strength value 1.33693(26) for B-like Ar. Additionally, Froese Fisher *et al.* [20] reported a line strength 1.3372 for B-like Ar. Froese Fisher *et al.* [20] further extended their calculations for the B-like isoelectronic sequence until $Z = 42$. As seen from Table 3.2 our results also agree with B-like Fe and B-like Mo. Our results of the line strengths for all other systems under present study are in agreement with other available theories. The only exception is with the relativistic coupled-cluster calculations of Nandy [77] for which the line strength of 1.356(5) in F-like Ar is overestimated and the line strength of 1.3270 in F-like Fe of Nandy and Sahoo [82] is underestimated. This may be due to the incorrect handling of intruder states in the implementation of coupled-cluster theory in open shell systems [87]. Overall, our calculations have reached an accuracy of $10^{-4} - 10^{-5}$ for the QED sensitive $M1$ line strengths between the fine structure levels of the same configuration. As a result, the present calculations provide a theoretical prerequisite for a test of QED effects in the line strengths of various ions.

In Table 3.4 we present the lifetimes τ_{pres} (in seconds) calculated for the $(2s^2 2p)$ $^2P_{3/2}$ level in B-like ions, the $(2s^2 2p^5)$ $^2P_{1/2}$ level in F-like ions, the $(3s^2 3p)$ $^2P_{3/2}$ level in Al-like ions as well as for the $(3s^2 3p^5)$ $^2P_{1/2}$ level in Cl-like ions. Here, τ_{exp} are experimental lifetimes and respective experimental uncertainties are given in parentheses. A^{M1} is the present transition rate from the $M1$ channel. We used the best available transition energies from the literature for the calculation of the transition rate. For B-like ions we applied the transition energies from the rigorous QED treatment of Artemyev *et al.* [8, 10], and for the rest of the ions we used transition energies from the NIST database [88]. Here A^{E2} is the transition rate from the $E2$ channel in length form. For the $E2$ transition rate, we make use of the same wave function expansion as for the $M1$ transition rate, in addition to that the length and the velocity gauges of the $E2$ line strength were in good agreement. Let us note that the present uncertainties in transition rates and lifetimes are due to uncertainties in the calculation of the $M1$ line strengths only. They are given within the parentheses. For the present level of accuracy, the uncertainties due to the $E2$ transition channel are very small. However, the uncertainties in the transition energies will increase total uncertainties in our calculations accordingly.

Table 3.4: Lifetimes τ_{pres} (in seconds) calculated for the $(2s^22p)\ ^2P_{3/2}$ level in B-like ions, the $(2s^22p^5)\ ^2P_{1/2}$ level in F-like ions, the $(3s^23p)\ ^2P_{3/2}$ level in Al-like ions and the $(3s^23p^5)\ ^2P_{1/2}$ level in Cl-like ions compared with experimental lifetimes (τ_{exp}). A^{M1} is the present transition rate (in s^{-1}) from the $M1$ channel and A^{E2} is the transition rate (in s^{-1}) from the $E2$ channel. The values of the transition energy used for the present lifetime calculations are given in cm^{-1} and corresponding transition wavelengths λ in Å. The uncertainties involved in the calculation of transition rate and lifetime arising due to uncertainties in the line strengths are given within the parentheses. The numbers given in the square brackets denote powers of 10.

Ions	Energy	λ	A^{M1}	A^{E2}	τ_{pres}	τ_{exp}
B-like						
Ar^{13+}	22656.92	4413.663	1.0487(02)[+02]	1.86[-03]	9.5354(20)[-03]	9.573(4)(5)[-03][1]
						8.7(5)[-03][2]
						9.12(18)[-03][3]
						9.70(15)[-03][4]
Fe^{21+}	118310.243	845.235	1.4893(03)[+04]	1.37[+00]	6.7141(11)[-05]	
Mo^{37+}	964437.459	103.687	7.9810(60)[+06]	6.00[+03]	1.2520(09)[-07]	
W^{69+}	11802649.713	8.473	1.3985(20)[+10]	1.25[+08]	7.0874(10)[-11]	
Al-like						
Fe^{13+}	18852.5	5304.336	6.0455(33)[+01]	1.49[-02]	1.6537(09)[-02]	1.6726(+20/-10)[-02][5]
						1.7(2)[-02][6]
						1.674(12)[-02][7]
						1.752(29)[-02][8]
Mo^{29+}	204020	490.148	7.6299(74)[+04]	1.67[+02]	1.3078(12)[-05]	
W^{61+}	2933400	34.090	2.2008(34)[+08]	6.30[+06]	4.4174(70)[-09]	
F-like						
Ar^{9+}	18067.494	5534.802	1.0639(04)[+02]	2.11[-03]	9.3994(33)[-03]	9.32(12)[-03][4]
Fe^{17+}	102579	974.858	1.9428(10)[+04]	1.94[+00]	5.1466(26)[-05]	
Mo^{33+}	886305	112.828	1.2432(12)[+07]	9.77[+03]	8.0372(79)[-08]	
W^{65+}	11202000	8.927	2.4097(57)[+10]	2.16[+08]	4.1131(98)[-11]	
Cl-like						
Fe^{9+}	15683.14	6376.274	6.9615(93)[+01]	1.52[-02]	1.4362(19)[-02]	1.42(2)[-02][9]
						1.441(14)[-02][10]
						1.364(25)[-02][8]
Mo^{25+}	186950	534.902	1.1746(13)[+05]	2.41[+02]	8.4959(96)[-06]	
W^{57+}	2796000	35.765	3.8190(94)[+08]	1.05[+07]	2.5485(65)[-09]	

[1] HD-EBIT experiment by Lapierre *et al.*. [13].

[2] NIST-EBIT experiment by Serpa *et al.*[89].

[3] ECRIS in a Kingdon ion trap experiment by Moehs *et al.* [90].

[4] LLNL-EBIT by Träbert *et al.* [91].

[5] HD-EBIT experiment by Brenner *et al.* [14].

[6] ECRIS in a Kingdon ion trap experiment by Smith *et al.* [92].

[7] LLNL-EBIT experiment by Beiersdorfer *et al.* [93].

[8] ECRIS in a Kingdon ion trap by Moehs and Church [94].

[9] HD-EBIT experiment by Brenner *et al.* [95].

[10] TSR measurements at the Max Planck Institute for Nuclear Physics, Heidelberg, Germany by Träbert *et al.* [96].

As seen from Table 3.4, our predicted lifetimes for B-like Ar and for Al-like Fe disagree with both experiments at the HD-EBIT [13, 14]. In contrast, the comparison of our predicted lifetime for F-like Ar with the experiment at the LLNL-EBIT [91] and for the lifetime of Cl-like Fe with the experiment at the HD-EBIT [95] shows very good agreement. For Cl-like Fe, our lifetime also agrees well with the extrapolated lifetime of Träbert *et al.* [96] which is resulted in an experimental study along Cl-like Co, Ni and Cu ions. These experiments with an uncertainty larger than 0.5% are however not sensitive enough to test the underlying relativistic correlations and the leading QED effects. New experiments with the soft x-ray free electron laser (FLASH) and a new EBIT [97] along with the pump probe x-ray laser experiments [26] are hopeful to provide experimental data for the transitions with short lifetimes in so far inaccessible energy ranges. We believe that our calculations will support such future experiments for transitions with different frequencies and lifetimes.

4 $E1$ dipole allowed transition in Be-like carbon

In this chapter, we shall present a detailed calculation of the line strength of the $1s^22s2p\,{}^1P_1 - 1s^22s^2\,{}^1S_0$ transition in Be-like carbon in the prospect of high precision experiment [98]. This transition within the same shell ($\Delta n = 0$) and in the low charge state of the ion is highly correlated. Therefore, we develop various electron correlation models and use orthogonal and nonorthogonal set of orbitals for the initial and final states in these correlation models. Generally, the $E1$ line strength is computed with two operators, referred to as the Babushkin and the Coulomb form, which in the non-relativistic limit correspond to the length and velocity form. In this thesis, we will refer to them as length and velocity form, respectively. We shall discuss that the accuracy assessment based only on an agreement between the gauges might be overestimated. For this reason, we shall estimate the uncertainty from the differences between the results obtained within all the correlation models that are developed in present work. Moreover, we shall demonstrate that the gauge invariant finite nuclear mass effect to the line strength is achieved after taking into account the recoil correction to the transition operator.

The following parts of the chapter are structured as follows. In Sec. 4.1, we present a brief introduction of the experimental proposal for CRYRING at ESR (at GSI Darmstadt). In Sec. 4.2 we present the underlying theory for calculation of the line strength. A detail of the correlations models and results obtained are explained in Sec. 4.3. In Sec. 4.4, we present theoretical methods for the finite nuclear mass effect. In the final section of this Chapter, we compare and discuss the obtained results with other theories and experiments.

4.1 Experimental proposal for CRYRING at ESR

A schematic diagram of the proposed pump-probe experiment is shown in Fig 4.1. The system is excited from the ground state to a short-lived excited state by the pump pulse via a dipole $E1$ transition. The population of this excited state is then probed by photoionization with a second temporally delayed probe pulse. By measuring the ionization signal (changed charge state) via the delay of both pulses the excited state lifetime can be determined. A first experiment on the Be-like carbon ions has been proposed to be performed at CRYRING at GSI Darmstadt [27]. Here the photon energy of both pulses is in the XUV spectral region. The pump and the probe pulses will be delivered by a table-top XUV source based on high harmonic generation [99]. By splitting the pulses delivered by a high repetition rate femtosecond laser system, two well synchronized pulses will be generated and subsequently frequency-converted to the XUV via high harmonic generation in two gas jets, as illustrated in Fig 4.2. The overlap of ion beam and laser beams will be ensured by scrapers along a ~ 3 m long interaction region. The changed charge

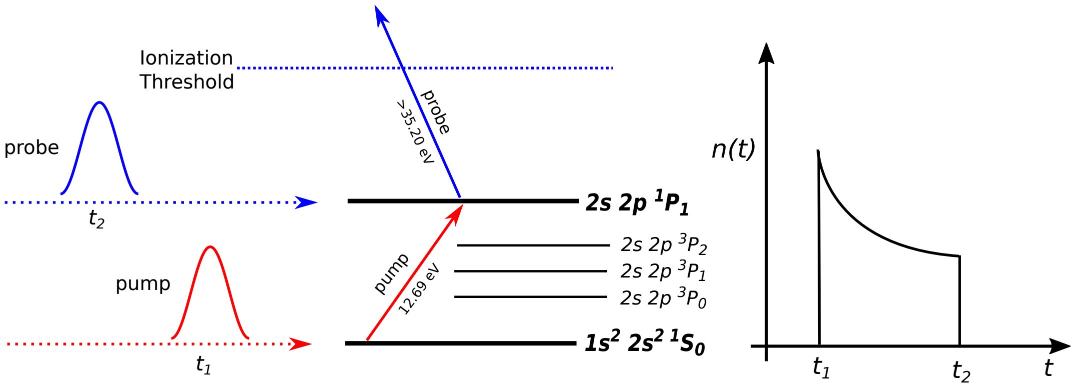

Figure 4.1: Scheme of a pump-probe experiment for atomic lifetime measurements of the $1s^22s2p\ ^1P_1$ state in Be-like carbon. At time t_1 the XUV-pump pulse excites the $1s^22s^2\ ^1S_0$ ground state of the Be-like carbon sample to the $1s^22s2p\ ^1P_1$ excited state. The population $n(t)$ of the excited state $^1P_1$ decays then exponentially. A second and temporally delayed XUV-probe pulse probes the rest population of the excited state at time t_2 by ionizing Be-like carbon ion and maps out the exponential curve from which the decay rate is determined.

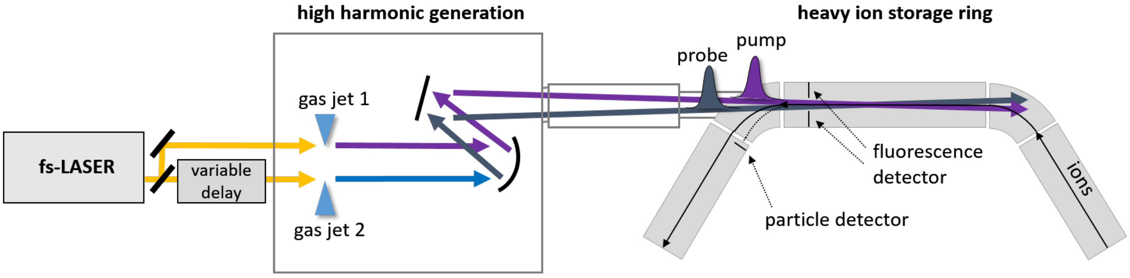

Figure 4.2: Schematic drawing of a XUV-pump XUV-probe experiment on Be-like carbon ions at CRYRING at GSI Darmstadt.

state of the ions will finally be detected by a particle detector within the subsequent dipole magnet. Within the frame of the ions, which move anticollinearly to the XUV pulses, the photon energy can be effectively tuned onto resonance via Doppler tuning [100]. In this way, the transition energy can be measured as well.

The pump-probe measurement promises to reach $\sim$ 100 fs absolute and 10^{-4} precision with a few-ns delay line and thus will provide novel sensitive tests for state-of-the-art atomic structure calculations. Note that the high energy storage ring (HESR) at the future FAIR facility will provide relativistic ion beams with a Doppler-shift up to an order of magnitude. Thus, similar experiments can be performed with a large variety of highly-charged ions including H-, He-, Li- and Be-like ions.

4.2 Basic formulas

The electric dipole transition probability from an upper state k to a lower state j is expressed in terms of the line strength as

$$A_{kj}^{E1} = \frac{4}{3}\frac{\omega^3}{c^3}\frac{S}{2J_k+1} , \tag{4.1}$$

where c is the speed of light and ω the transition energy between the two states. The line strength S is square of the reduced non-diagonal matrix element (2.35) given as

$$S = |\langle\Psi(\Gamma_k;\pi_k J_k)||\boldsymbol{T}^{E1}||\Psi(\Gamma_j;\pi_j J_j)\rangle|^2 , \tag{4.2}$$

Here, $\boldsymbol{T}^{E1}$ is $E1$ transition operator [59]

$$T_M^l = \frac{\sqrt{2\pi}c}{\omega}\sum_i^N \Big[-\sqrt{6}j_1(\omega r_i/c)Y_{1M}(\boldsymbol{n}_i) + 3j_2(\omega r_i/c)c\boldsymbol{\alpha}_i \cdot \boldsymbol{Y}_{1M}^2(\boldsymbol{n}_i)\Big] , \tag{4.3}$$

in the length gauge and

$$T_M^v = \frac{\sqrt{2\pi}c}{\omega}\sum_i^N \Big[-\sqrt{2}j_0(\omega r_i/c)c\boldsymbol{\alpha}_i \cdot \boldsymbol{Y}_{1M}^0(\boldsymbol{n}_i) + j_2(\omega r_i/c)c\boldsymbol{\alpha}_i \cdot \boldsymbol{Y}_{1M}^2(\boldsymbol{n}_i)\Big] , \tag{4.4}$$

in the velocity gauge. Here, ω is the transition energy, Y_{JM} are the spherical harmonics, $\boldsymbol{Y}^L_{JM}$ are the spherical vectors, and $j_J(\omega r/c)$ is the spherical Bessel function. In order to investigate the dependence of the line strength on the transition energy we expand the Bessel functions $j_J(\omega r/c) \approx (\omega r/c)^J/(2J+1)!!$, so called the long-wavelength approximation $\omega/c \ll 1$, and retain only the leading term in the power series expansion. In such a way the line strength takes a form:

$$S^l \approx \left| \left\langle \Psi(\Gamma_k;\pi_k J_k) || \sum_i^N \boldsymbol{r}_i || \Psi(\Gamma_j;\pi_j J_j) \right\rangle \right|^2 , \tag{4.5}$$

in the length gauge and

$$S^v \approx \frac{c^4}{\omega^2} \left| \left\langle \Psi(\Gamma_k;\pi_k J_k) || \sum_i^N \boldsymbol{\alpha}_i || \Psi(\Gamma_j;\pi_j J_j) \right\rangle \right|^2 , \tag{4.6}$$

in the velocity gauge. From the expressions (4.5) and (4.6) one can see, that the leading terms of the line strength in the length form is insensitive to transition energy whereas in the velocity form it is proportional to ω^{-2}. Based on these observations one can introduce the semi-empirical correction to the line strength in the velocity gauge by adjusting the transition energy to a more accurate, e.g., experimental, value, i.e., $\Delta S^v = (\omega^2 - \omega^2_{\mathrm{exp}})/\omega^2_{\mathrm{exp}}\, S^v$. Such a correction allows to take partially into account the missing correlation contributions. The line strength in the velocity gauge adjusted in this way $S^v_{(\mathrm{exp})}$ is typically much closer to the value in the length gauge S^l. Generally, the gauge invariance should be restored when all correlation effects are taken into account, both for the transition matrix element and transition energy, which was explicitly demonstrated in the framework of the relativistic many-body perturbation theory [101] and QED formalism [102]. In view of this, the excellent agreement between the gauges after adjustment suggests that the remaining unaccounted correlation effects to the transition amplitude are rather small. As a result, the difference between the line strengths calculated in the length gauge and adjusted value in the velocity gauge is employed for the theoretical error estimation [103, 104]. However, it is still possible that the remaining unaccounted correlation effects bring not only the identity in the gauges, but also a shift to both the values an amount much larger than the difference between the gauges after adjustment.

4.3 Correlation models

In a view of an absence of strong criteria for the uncertainty estimation of the calculated line strength, we performed the MCDHF calculations for different correlations models. Among those models, we choose only four models based on the accuracy criterion for the transition energy as it is compared with the experimental energy as well as the agreement between the two gauges of the line strength. These four models were based on a separate and simultaneous (orthogonal and nonorthogonal) set of orbitals for the ground and excited states. In each model, the correlations were incorporated by systematically extending the calculations as describes in Sec. 2.5. Here the reference configurations for the first three models were $\{1s^2 2s^2,\, 1s^2 2p^2\}$ for the ${}^1S_0$ ground state and $\{1s^2 2s2p\}$ for the ${}^1P_1$ excited state. For the fourth model, the reference configurations were increased and we explain its details later in this section. The calculations were extended by expanding the basis set of CSFs using the active set approach as describes in Sec. 2.5.

We now explain how valence-valence (VV), core-valence (CV) and core-core (CC) correlations were incorporated. We started to expand the basis set by adding the CSFs that are generated from the configurations $1s^2 nln'l'$ which are resulted from SD excitations from outer shells of the reference configuration. These CSFs account VV correlations and the calculations are named as VV calculations. To each layer of VV correlation calculations, we then added CSFs of the configurations $1s2snln'l' + 1s2pnln'l'$ which arise from the single excitation from the $1s^2$ core with or without another excitation from the valence shells. These added CSFs account for the CV correlations and the calculations are called VV+CV. Now with each layer of VV+CV correlation calculations, the correlations of two-electron excitations from the $1s^2$ core were included to account for the CC correlations. These additional CSFs arise from the configurations $2s^2 nln'l' + 2p^2 nln'l'$ for the ${}^1S_0$ state and $2s2pnln'l'$ for the ${}^1P_1$ state. These correlation calculations are named as VV+CV+CC calculations. In all VV, VV+CV and VV+CV+CC calculations, the active set of orbitals was spanned by the orbitals with principal quantum number $n, n' \leq 15$ and with azimuthal quantum number $l, l' \leq 7$. Finally, the basis set of CSFs was expanded by appending CSFs with configurations arising from SDTQ excitations from the reference configurations. In the SDTQ excitations the number of CSFs increased very rapidly with the increasing number of orbitals in the active set which limits the numerical stability and available hardware resources. So the SDTQ excitations were limited only with $n, n' \leq 5$ and $l, l' \leq 4$. These calculation were then extended with SD excitations with remaining layer of correlation orbitals with $n, n' \leq 15$ and $l, l' \leq 7$. We name these final set of calculations as VV+CV+CC:SDTQ.

4.3.1 Model 1

In this model the VV and VV+CV calculations were performed by utilizing the OL scheme for the ground and excited state, i.e., for both states orbitals were separately optimized, whereas for the VV+CV+CC as well as VV+CV+CC:SDTQ calculations the spectroscopic orbitals and the correlation orbitals with $n = 3$ were simultaneously optimized using the EOL scheme. Then the calculations after $n = 3$ were extended with a separate set of correlation orbitals (the OL scheme). This model accounts for the correlations in a similar manner as those presented by Jönsson and Froese Fischer [32]. The only difference is that Jönsson and Froese Fischer performed VV+CV+CC:SDTQ calculations with SDTQ excitation until $n = 3$ only and extended their calculations from $n > 3$ with VV+CV type of correlations only.

In Fig. 4.3 (upper plot) we compare the present calculations of Model 1 with Jönsson and Froese Fischer results in [32]. The line strength in length and velocity form is plotted against increasing n of the active set size defining the wave function expansion in respective calculations. It is clearly evident that their two gauges agree perfectly at $n = 8$ once the experimental energy adjustment was applied. Explicitly, the line strength calculated by Jönsson and Froese Fischer [32] amounts to 2.4376 in the length gauge and 2.4366 in the velocity gauge after adjustment, which leads to a tabulated final value 2.4376(13). Despite we cannot explicitly reproduce these calculations, our evaluations show the similar effect at $n = 7$ active set layer, where the results obtained in the length and velocity (adjusted) gauges approach each other. However, when the active set size is further extended, one can clearly see that after $n = 7$ layer the results first drift apart and then, again, approach each other but at some different position. These observations lead us to the following conclusions. First, the agreement between gauges might be of an accidental character and, therefore, second, the difference between results in the length and velocity (adjusted) gauges should be very carefully used as a criterion for the error estimation.

Let us mention here another important observation. From the basic theory

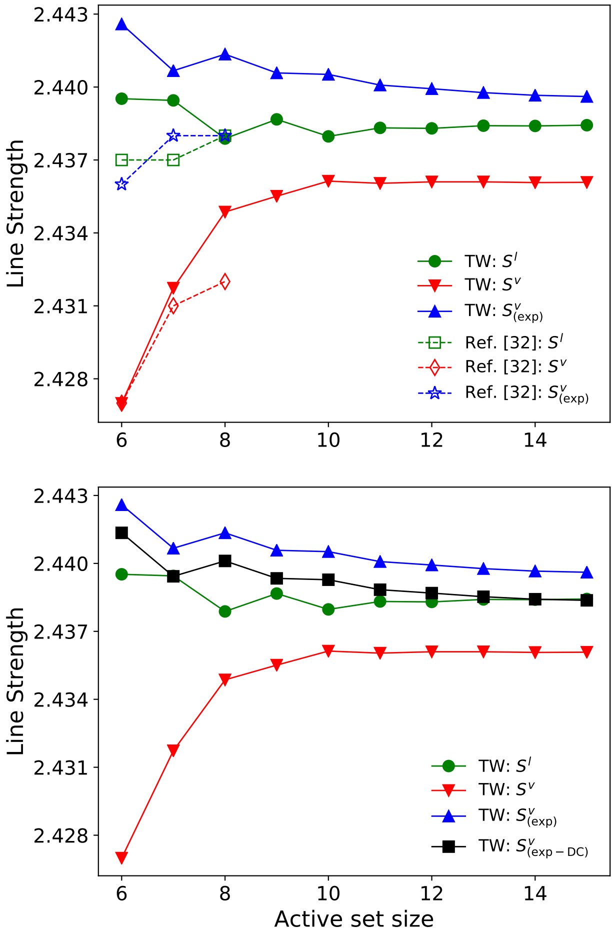

Figure 4.3: Comparison of the line strengths evaluated according to the Model 1 (TW) as a function of active set size of the orbitals with the results of Jönsson and Froese Fischer [32]. The green circles, red down triangles, and blue upper triangles display the present calculations in the length gauge S^l as well as in velocity gauges before S^v and after adjustment $S^v_{(\mathrm{exp})}$ to the experimental transition energy ω_{exp}, respectively. The green hollow squares, red hollow diamonds, and blue hollow stars are corresponding values taken from Ref. [32].

[101, 102], it is clear that the adjustment should be made to the transition energy which corresponds to the difference of the eigenvalues of the Dirac-Coulomb Hamiltonian in Eq. (2.3). Therefore, we calculate a so-called experimental-Dirac-Coulomb transition energy $\omega_{\mathrm{exp-DC}}$ as a difference of the experimental value ω_{exp} and the contributions beyond the Dirac-Coulomb approximation, i.e., the Breit interaction, recoil, and QED corrections. The $\omega_{\mathrm{exp-DC}}$ energy is, thus, experimentally deduced fully correlated Dirac-Coulomb transition energy. At this end, we compare

Table 4.1: Transition energies ω (cm^{-1}) and line strengths S (a.u.) for the $1s^22s2p$ $^1P_1 - 1s^22s^2\ ^1S_0$ transition in Be-like carbon as functions of the active set calculated within Model 1. The line strengths in the length gauge (S^l) are compared with those in the velocity gauge ab initially calculated (S^v) and after adjustment to the experimental energy $\omega_{\rm exp}$ ($S^v_{\rm (exp)}$) and to the experimental-Dirac-Coulomb energy $\omega_{\rm exp-DC}$ ($S^v_{\rm (exp-DC)}$). The experimental transition energy is taken from Ref. [88], while the experimental-Dirac-Coulomb energy is evaluated by subtracting the Breit, recoil, and QED corrections from the experimental transition energy.

Active set	ω	S^l	S^v	$S^v_{\rm (exp)}$	$S^v_{\rm (exp-DC)}$
DHF	112 958	2.34092	1.65645	2.01753	2.01651
$3s3p3d$	104 094	2.51432	2.36757	2.44884	2.44759
$4s4p4d4f$	103 116	2.45884	2.38001	2.41568	2.41446
$5s5p5d5f5g$	102 804	2.44978	2.40435	2.42565	2.42442
$6s6p6d6f6g6h$	102 680	2.43952	2.42699	2.44259	2.44135
$7s7p7d7f7g7h7i$	102 540	2.43945	2.43173	2.44067	2.43943
$8s8p8d8f8g8h8i8k$	102 488	2.43788	2.43486	2.44135	2.44011
$9s9p9d9f9g9h9i9k$	102 459	2.43867	2.43551	2.44058	2.43934
$10s10p10d10f10g10h10i10k$	102 444	2.43797	2.43613	2.44052	2.43928
$11s11p11d11f11g11h11i10k$	102 437	2.43832	2.43604	2.44008	2.43884
$12s12p12d12f12g12h12i10k$	102 432	2.43830	2.43610	2.43993	2.43869
$13s13p13d13f13g13h13i10k$	102 429	2.43841	2.43610	2.43977	2.43853
$14s14p14d14f14g14h14i10k$	102 427	2.43840	2.43607	2.43966	2.43842
$15s15p15d15f15g15h15i10k$	102 426	2.43843	2.43608	2.43961	2.43837
Due to other models	-15				
Breit	-3				
Recoil	-13				
QED	-10				
Total	102 385				
Exp	102 352				
Exp-DC	102 378				

in Table 4.1 as well as in Fig. 4.3 (lower plot) the line strengths in the length gauge (S^l) and in the velocity gauge (*ab initio*) (S^v) with the adjusted to $\omega_{\rm exp}$ ($S^v_{\rm (exp)}$) and to $\omega_{\rm exp-DC}$ ($S^v_{\rm (exp-DC)}$) values. As one can see from this comparison the values adjusted to the experimental-Dirac-Coulomb energy are much close to the results in the length gauge. In particular, for $n = 15$ layer the relative difference between the gauges amounts to 2×10^{-5}. However, as we have mentioned at the end of Sec. 4.2 that the agreement between the gauges cannot be uniquely used for the accuracy assessment. For this reason, in the next subsections, we investigate also other correlation models.

4.3.2 Model 2

Within this model, both the spectroscopic and the correlations orbitals were separately optimized using the OL scheme for all type of correlations. Hence generated orbitals for both states were not quite orthogonal with each other, which makes the implementation of standard Racah algebra difficult for the calculation of transition amplitude. To deal with this complication, a transformation to a biorthonormal basis was applied together with the counter transformation of the expansion coefficients as explained in Sec. 2.7.

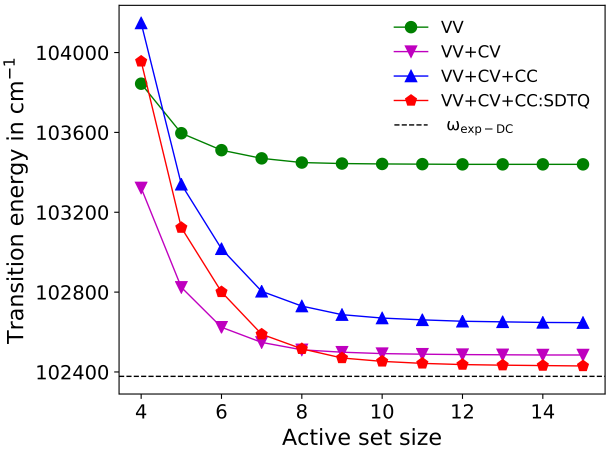

Figure 4.4: Extent of different correlations effects to the transition energy with respect to the increasing n of the active set size defining the wave function expansion for the Model 2 calculations. The green circles represent VV correlations, magenta down triangles represent VV+CV, blue upper triangles represent VV+CV+CC, red-pentagons represent VV+CV+CC:SDTQ correlations. Please see the text for the details of different type of the correlations.

The calculations within this model show the importance of a common set of orbitals for the core correlations in the framework of MCDHF approach. For the CC effects, it is commonly accepted that these are more balanced if a common orbital basis is used for describing both the states involved in the transition and hence resulting transition energies are more accurate [105, 106]. This is also obvious from Fig. 4.4 where the evaluation of different correlations effects to the transition energy are shown with respect to the increasing n of the active set size defining the wave function expansion for the Model 2 calculations. Here the blue upper triangles representing VV+CV+CC correlation results are worse than the magenta down triangles representing VV+CV correlations. However, it is obvious from the red-pentagons representing VV+CV+CC:SDTQ in Fig. 4.4 that we get the best agreement of the transition energy with the experiment when the TQ excitations are included with SD excitations in the CC correlations. The difference of the final values of the energy of VV+CV+CC:SDTQ calculations with Model 1 and Model 2 is only 0.004%, whereas the length form of the line strength from both models varies only by 0.01%. The fact that TQ contributions are very important is also noticed from the results of Chen, Cheng and Johnson [35] who have also used TQ excitations in building a common set of orbitals in their RCI calculations based on B-spline basis.

4.3.3 Model 3

Within this model, both the spectroscopic orbitals and correlations orbitals were simultaneously optimized for the ground and excited states using the EOL scheme for all type of correlations. The so obtained orbitals for both states were orthogonal to each other. As it has been highlighted by Chen, Cheng and Johnson [35] and Savukov [36] that small orbital overlap corrections due to a non-diagonal set of orbitals for the initial and final states should not be ignored. Our correlation Model 3 helps to address this issue.

4.3.4 Model MR

In this model, the set of spectroscopic reference configurations were expanded to account the missing correlations due to limited SDTQ excitations. We name it as multi-reference (MR) model. The configurations in MR were expanded in such a way that the CSFs for the MR set had the largest expansion coefficients in the wave functions that were generated by VV+CV+CC:SDTQ calculations of Model 3. For the $^1S_0$ ground state the resulting MR set was $\{1s^22s^2, 1s^22p^2, 1s^23p^2, 2s^23s^2, 2s^23p^2, 1s^23d^2\}$ and for the $^1P_1$ excited state the resulting MR set was $\{1s^22s2p, 1s^22p3d, 2s2p3s^2, 2s2p3p^2\}$. All the orbitals occupied in MR set were spectroscopically treated in the lowest order of approximation. Then the correlation orbitals were treated in the same way as those of Model 3 using the

EOL scheme.

4.3.5 Models: summary

Our approach with either a common or two separate set of orbitals for the ground and excited states combines the strengths and weaknesses of the previous calculations which provide the uncertainty of the order of 10^{-3} [32, 35, 36]. The orbitals in the common set for both states are orthogonal to each other and there is no orbital overlap for the evaluation of the transition amplitude. At the same time, our procedure of two different sets of orbitals for each state has the advantage that the electron relaxation effects are automatically included to a large extent.

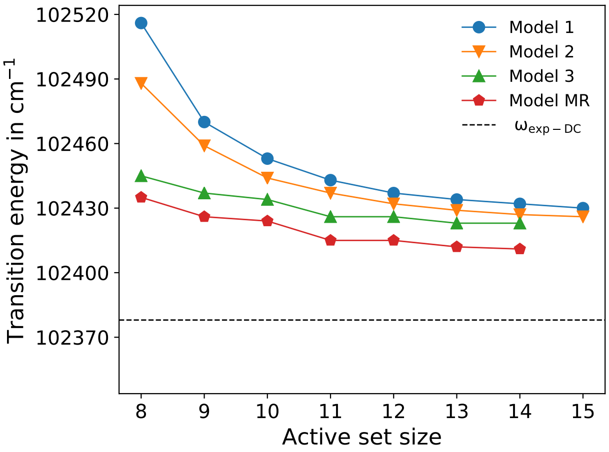

Figure 4.5: Convergence of transition energy with respect to the increasing n of the active set size defining the wave function expansion for the VV+CV+CC:SDTQ calculations of different correlation models. Please see the text for the details of the VV+CV+CC:SDTQ calculations.

In all our correlation models the overall convergence trends and behavior of the inner and outer electron correlations are consistent with each other. In Fig. 4.5 we present the convergence of the transition energy with respect to the increasing n of the active set size defining the wave function expansion for the VV+CV+CC:SDTQ calculations from all the correlation models under present study. For the Model 3 and MR we could not get the converged orbitals for $n = 15$. The first three models vary just with a difference of maximum of 6 cm^{-1}. But for Model MR we get 15 cm^{-1} better results and this is obvious due to the inclusion of higher-order correlations in

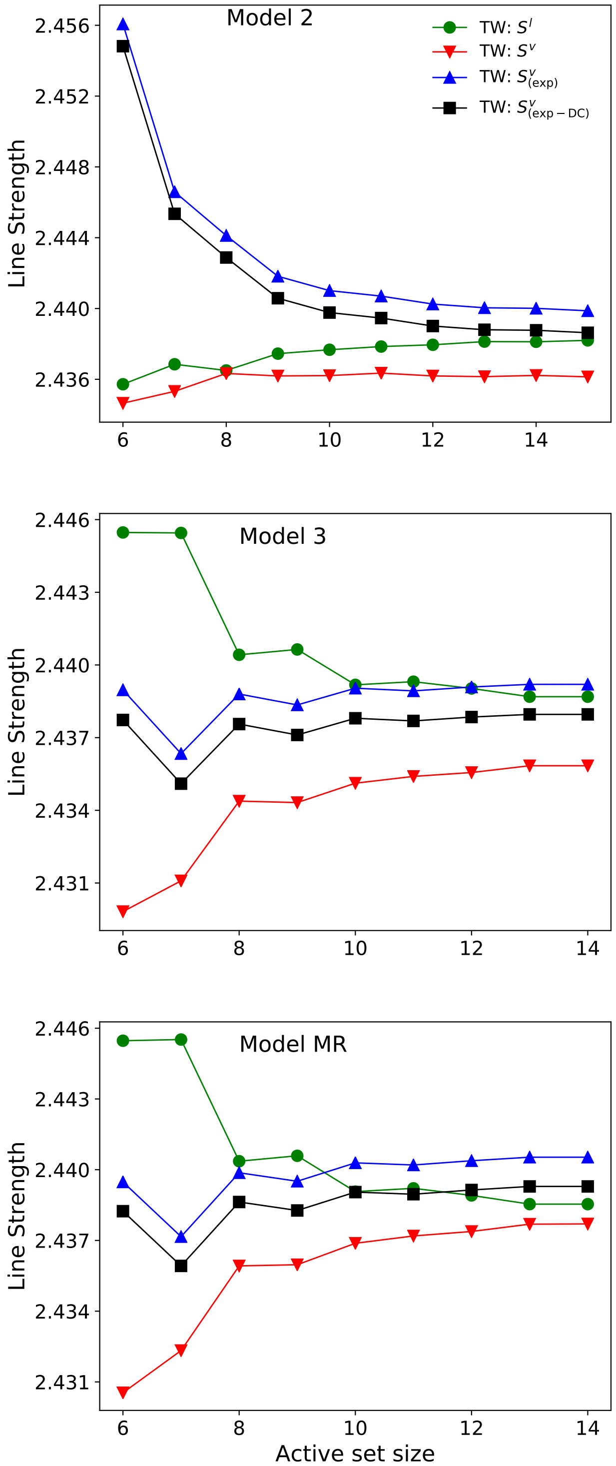

Figure 4.6: Line strength for the for the VV+CV+CC:SDTQ calculations from the Model 2, Model 3 and Model MR plotted similarly as that of Fig. 4.3. In each subfigure, the green circles are the line strength S^l in length form, red down triangles are *ab initio* S^v velocity from, blue upper triangles are $S^v_{(\mathrm{exp})}$ velocity form adjusted the experimental transition energy ω_{exp} and black squares are $S^v_{(\mathrm{exp-DC})}$ velocity from adjusted the experimental-Dirac-Coulomb transition energy $\omega_{\mathrm{exp-DC}}$ (see text).

this model.

In Fig. 4.6 we present the line strength for the VV+CV+CC:SDTQ correlations calculated within Model 2, 3, and MR in a similar way as explained in Sec. 4.3.1 and Fig. 4.3 (lower plot). From these plots, one can clearly see that in all models the line strength in the velocity adjusted to the experimental-Dirac-Coulomb energy agrees with the length gauge result much better than the adjusted to the pure experimental energy. This also confirms our expectations originated from the basic principles as stated at the end of Sec. 4.3.1. In order to get the final (Dirac-Coulomb) line strength value the results of the length gauge and adjusted to the experimental-Dirac-Coulomb energy velocity gauge obtained at the maximum active set size are analysed.

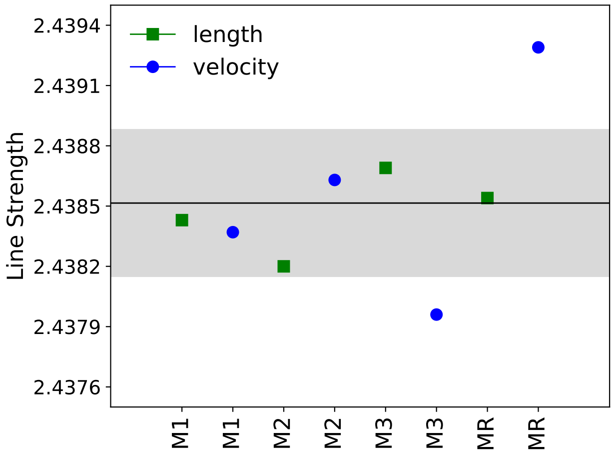

Figure 4.7: Line strength of the $1s^22s2p\ ^1P_1\ -\ 1s^22s^2\ ^1S_0$ transition in Be-like carbon plotted against the present Models. Green squares represent to the length forms and blue circles to the velocity forms. The black solid line is the average of the both length and velocity forms. The gray shaded region is one standard deviation from the black line.

The employed data from all the correlation models are summarized in Table 4.2 and Fig. 4.7. As one can see from these data, despite the extraordinary agreement between gauges, e.g., in Model 1, one cannot use it for the uncertainty estimation. The reason for this has been explained at the end of Sec. 4.2 and confirmed now by the calculations in other models, which predict the quite larger spread of the results than given by the difference of the gauges. We use these scatter of the line strength data to predict the final value of the line strength accounting only the correlations

Table 4.2: ω is the Dirac-Coulomb transition energy (cm^{-1}). S^l and $S^v_{(\mathrm{exp-DC})}$ are the Dirac-Coulomb line strengths in the length gauge and in the velocity gauge adjusted to $\omega_{\mathrm{exp-DC}}$ energy (see text), in a.u.

Label	ω	S^l	$S^v_{(\mathrm{exp-DC})}$
Model 1	102426	2.43843	2.43837
Model 2	102430	2.43820	2.43863
Model 3	102423	2.43869	2.43796
Model MR	102411	2.43854	2.43929
Final		2.43851(37)	

as 2.43851(37). It is represented in Fig. 4.7, as the black solid line which is average of all the values plotted. We find rather conservative to assess the uncertainty as one standard deviation of the scattered data. It is shown as a gray shaded region in Fig. 4.7. Such kind of an error estimation is further supported by the fact that it covers all the values obtained in the length gauge, which is known to be more reliable.

4.4 Nuclear recoil correction

Once the line strength is calculated, including all the major correlation contributions, the finite nuclear mass (nuclear recoil) contribution was added as a correction given as

$$\Delta S_{\mathrm{rec}} = \Delta S_{\mathrm{rec,en}} + \Delta S_{\mathrm{rec,wf}} + \Delta S_{\mathrm{rec,op}}, \tag{4.7}$$

where the first two terms on the right side in Eq. (4.7) are the corrections in the line strength due change in energy and wave functions, respectively, causing due to the nuclear recoil effect. These corrections were calculated by correcting the Dirac-Coulomb Hamiltonian (2.3) for lowest order nuclear motional corrections of NMS and SMS as described in Sec. 2.6.3.

It is also important, however, to take into account the recoil correction to the transition operator, i.e., the third term in Eq. (4.7). Previously, it was considered in many studies [107–110] for the $E1$ transitions and for the $M1$-decay [17]. Starting from the non-relativistic Hamiltonian for N electrons and the nucleus, we obtain the following recoil corrections to the $E1$ transition operator:

$$\Delta \boldsymbol{T}^{l}_{\text{rec}} = -\frac{Z-N}{M+N}\sum_{i=1}^{N}\boldsymbol{r}_i \tag{4.8}$$

in the length gauge and

$$\Delta \boldsymbol{T}^{v}_{\text{rec}} = -\frac{Z}{M}\frac{1}{\omega}\sum_{i=1}^{N}\boldsymbol{p}_i \tag{4.9}$$

in the velocity gauge. From these expressions one can easily come to the corresponding corrections to the line strength

$$\begin{aligned}\Delta S^{l}_{\text{rec,op}} &= 2\text{Re}\Big\{\langle\Psi(\Gamma_k;\pi_k J_k)||\boldsymbol{T}^{l}||\Psi(\Gamma_j;\pi_j J_j)\rangle \\ &\times \langle\Psi(\Gamma_k;\pi_k J_k)||\Delta\boldsymbol{T}^{l}_{\text{rec}}||\Psi(\Gamma_j;\pi_j J_j)\rangle\Big\} \\ &\approx 2\frac{Z-N}{M}S^{l} \end{aligned} \tag{4.10}$$

and

$$\begin{aligned}\Delta S^{v}_{\text{rec,op}} &= 2\text{Re}\left\{\langle\Psi(\Gamma_k;\pi_k J_k)||\boldsymbol{T}^{v}||\Psi(\Gamma_j;\pi_j J_j)\rangle\right. \\ &\times \left.\langle\Psi(\Gamma_k;\pi_k J_k)||\Delta\boldsymbol{T}^{v}_{\text{rec}}||\Psi(\Gamma_j;\pi_j J_j)\rangle\right\} \\ &\approx 2\frac{Z}{M}S^{v}\,. \end{aligned} \tag{4.11}$$

In Table 4.3 different recoil contributions due to the energy, wave functions, and the operator are presented in the length and velocity gauges. Only after adding the term due to the change of the operator the total recoil correction starts to be gauge invariant. In view of this, we would recommend to introduce this contribution also

Table 4.3: The recoil corrections to the line strength originated from the energy and wave functions change, $\Delta S_{\text{rec,en+wf}}$, as well as due to the transition operator $\Delta S_{\text{rec,op}}$ calculated in the length and velocity gauges. The total gauge invariant recoil correction is presented in the last line. The values are in a.u.

Rec. correction	length	velocity
$\Delta S_{\text{rec,en+wf}}$	0.00000	−0.00089
$\Delta S_{\text{rec,op}}$	0.00045	0.00134
Total	0.00045	0.00045

to a next GRASP update.

4.5 Results and discussion

With the discussion above, we can obtain the final value of the line strength. In order to do so, we add to the Dirac-Coulomb value 2.43851(37) from Sec. 4.3 the recoil correction $\Delta S_{\mathrm{rec}} = 0.00045$ calculated in the previous section. In addition, we have to consider also other effects, such as the Breit interaction as well as QED. The Breit contribution has been calculated as follows. The frequency-independent Breit Hamiltonian has been added to the Dirac-Coulomb Hamiltonian given by Eq. (2.3). Then the RCI calculations have been performed within the correlation Model 1. Comparing further the obtained results with the corresponding Dirac-Coulomb values we get for the Breit contribution $\Delta S_{\mathrm{Breit}}$ 0.00030 and -0.00001 in the length and velocity gauge, respectively. Based on an analysis of the Breit contribution in the intercombination transition $2s2p\ {}^3P_1\ -\ 2s^2\ {}^1S_0$ in Be-like carbon [35] and on arguments presented in [111, 112], we attribute this difference to a consequence of the employed no-pair approximation. That means that the gauge invariance of the Breit contribution will be restored when the negative-energy states will be taken into account. On another hand, it was demonstrated [111, 112], that the negative-continuum affects dominantly only the result in the velocity gauge, while the result of the length gauge remains stable. In view of this, we add the Breit correction, $\Delta S_{\mathrm{Breit}} = 0.00030$, calculated in the length gauge to our final value. The remaining QED correction is estimated as $\alpha(\alpha Z)^2 \ln(\alpha Z)^{-1}$ [113, 114] to be 4×10^{-5}, which is much smaller than our uncertainty. As a result, our final value for the line strength reads 2.43926(37).

Once the line strength is calculated, it is straightforward to get the oscillator strength:

$$gf = \frac{2}{3}\omega S\,, \tag{4.12}$$

where g is the weight of upper state, and the lifetime of the $1s^2 2s2p\ {}^1P_1$ excited state:

$$\tau = \frac{1}{A_{ij}^{E1}}\,. \tag{4.13}$$

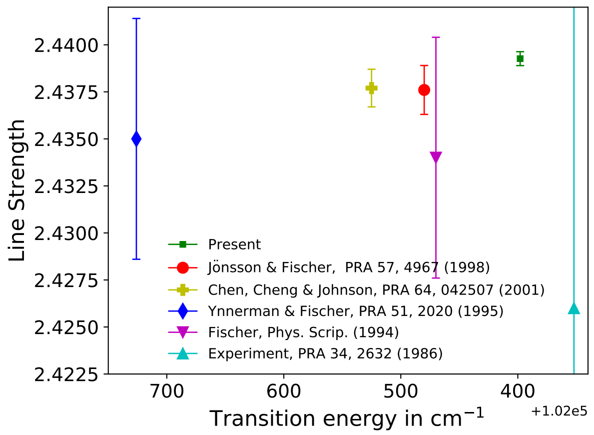

Figure 4.8: A comparison of the present line strength of the $1s^22s2p\ {}^1P_1\ -\ 1s^22s^2\ {}^1S_0$ transition in Be-like carbon with other theories and experiment.

Table 4.4: Comparisons between different calculations and experiments for the line strength of the $1s^22s2p\ {}^1P_1\ -\ 1s^22s^2\ {}^1S_0$ transition and the lifetime of the $1s^22s2p\ {}^1P_1$ excited state in Be-like carbon.

S [a.u.]	τ [ns]	Ref.
	Theories	
2.434(6)	0.5673(13)	[30]
2.435(6)	0.5671(13)	[31]
2.4376(13)	0.56650(30)	[32]
2.057	0.6713	[34]
2.4377(10)	0.56648(23)	[35]
2.4390(24)	0.56618(55)	[36]
2.436	0.5669	[33]
2.43926(37)	0.56612(9)	Present work
	Experiments	
2.09(1)	0.66(3)	[115]
2.16(2)	0.64(6)	[116]
2.09(2)	0.66(7)	[117]
2.76(1)	0.50(3)	[118]
2.42(1)	0.57(2)	[119]
2.426(45)	0.569(10)	[120]

Here the conversion to the lifetime form the line strength and vice versa is performed by using the experimental energy, $\omega = 102352.04$ cm^{-1} [88]. We note that the present uncertainty in the lifetime is only due to calculated line strength, since the uncertainty of the transition energy is expected to be much better than 1 cm^{-1} and this is far below the uncertainty of the line strength.

Fig. 4.8 and Table 4.4 compare the present results of calculated line strength and lifetime with other theories and experiments. Note that in the respective papers the values of oscillator strength is provided. We have converted the oscillator strength to the line strength using the energies mentioned in the respective papers. In Fig. 4.8, the experimental line strength reported by Reistad and Martinson [120] is plotted as a function of the experimental energy taken from the NIST database [88]. It is clear from Fig. 4.8 that our calculated energy is the closest to the experimental one. The present line strength or lifetime agrees very well with the CI+MBPT calculation of Savukov [36] and is in a fair agreement with the large-scale MCDF calculation of Jönsson and Froese Fischer [32] and the CI result of Chen, Cheng and Johnson [35].

It is obvious from the Table 4.4 that all the theoretical lifetimes except of Safronova *et al.* [34] are inside the error bar of the best available experimental lifetime of 0.569(10) ns [120]. However, the uncertainty of this measurement is still too large to distinguish between different theories. Therefore, we hope that the proposed experiment [27] will provide a new benchmark for testing the theories in the case of Be-like carbon.

5 $E1, M1, E2$ and $M2$ transitions in Cl-like Ni

In this chapter, we shall present a detailed computation of transition rates, oscillator strengths, and lifetimes for the first 31 lowest energy levels in Cl-like nickel (Ni XII) [121]. We shall take into account all allowed $E1$ and forbidden $M1$, $E2$, and $M2$ transitions among these levels. These lines arise from three configurations $3s^2 3p^5$, $3s3p^6$ and $3s^2 3p^4 3d$. For these ions, theoretical complexity arises due to the near degeneracy characteristic and strong mixing of multiplets with the same total angular momentum J and parity π. Moreover, the atomic properties of such ions with seven valence electrons are quite sensitive to electron correlations and their interplay with relativistic effects. So, the elaborate size of wave function expansion along with the incorporation of correlation effects and effects of relativity on equal footing should be included in a computational model. This, indeed, is computationally very expensive and needs special care in terms of numerical convergence for the desired atomic properties.

The reset of the chapter is structured as follows. A short description of our computational procedures and correlation models are described in Sec. 5.1. In Sec. 5.2 the obtained data are discussed and compared with other *ab initio* and semi-empirical calculations and with experiments where available.

5.1 Computational details

We performed the calculations for two odd parity states which belong to the $3s^2 3p^5$ ground configuration with total angular momentum $J = 1/2$ and $J = 3/2$ and for the 29 even parity states from the $3s3p^6$ and $3s^2 3p^4 3d$ configurations with total angular momenta in the range $J = 1/2, \ldots, 9/2$. We report two models of correlations calculations to investigate the importance of different non-dynamic and dynamic electron correlations effects [60]. In order to obtain the numerical convergence of the desired parameters, we systematically extended the configuration space using the method described in Sec. 2.5.

5.1.1 Model 1

In first model of calculations, the configurations $3s^23p^5$, $3s3p^6$ and $3s^23p^43d$ were taken as MR configurations for both even and odd parity states. In the lowest order approximation, the MCDHF calculations were performed simultaneously for even and odd parity states using the EOL scheme for the states in the MR set. All levels were given standard weights and a convergence for spectroscopic orbitals was achieved. In order to incorporate VV correlations only, we fixed the Ne like core ($1s^22s^22p^6$) i.e there is no virtual excitation from these orbitals. In subsequent calculations, we divided the states in six groups. One group for both of the odd states of the ground configuration and five separate groups of excited states with even parity corresponding to each total angular momentum $J = 1/2, \ldots, 9/2$. Here in active set approach [cf. Sec. 2.5], separate MCDHF calculations were performed for each group of states for each layer. In first correlation layer we included SDTQ excitation within $3l$ sub-shells. This step is referred to as the $n = 3$ calculations. Similar calculations for $n = 4, \ldots, 7$ are performed by including SD excitations from the MR configuration. For $n = 4$ the orbitals are *spdf* while for remaining higher layers we restrict ourselves to orbitals only up to g.

5.1.2 Model 2

In the second model of calculations, we took two separate MR sets for each even and odd parity symmetries. The configurations $3s^23p^5$, $3s3p^53d$, $3s^23p^33d^2$ and $3p^53d^2$ define MR set for the odd parity states and configurations $3s3p^6$, $3s^23p^43d$, $3s3p^43d^2$ and $3p^63d$ define MR set for the even parity states. In the lowest order approximation for this model, two separate MCDHF calculations for each parity were performed in EOL scheme for lowest 31 states by taking the weighted average of even and odd parity states. This lowest order approximation accounts for the nondynamic electron correlations that result from the close degeneracy of the orbitals [122]. For subsequent calculations, here again we divided the states into six groups in a similar way as in the first set of calculations. The rest of the approach for adding correlation layers is the same as in the first model of calculations but a single excitation from Ne-like core is also included in each correlation layer in order to incorporate CV correlations in addition to VV correlations. Here we name these VV+CV calculations as CV calculations. In this model of calculations the effects of SDTQ excitations within $3l$ were negligible, therefore we restricted ourselves to single and double excitations to all correlation layers with a maximum azimuthal quantum number of h. In this model, the size of configuration space grows very rapidly so we restricted ourselves only with those CSFs which have non zero Hamiltonian matrix elements with CSFs of configurations in the MR sets. In this way there was an almost 20% decrease in the total number of CSFs, nevertheless, the number of CSFs in the final odd and even state expansions was approximately two million, as given in Table 5.1.

Each of the MCDHF calculation in both models was followed by a RCI calculation where we added Breit interaction, effects of vacuum polarization and self energy corrections. Then the transition parameter for the $E1, M1, E2$, and $M2$ transitions between the optimized states were calculated from the of transition matrix elements (2.35). For electric multipole transitions ($E1, E2$), calculations are performed for both gauges i.e. the length and the velocity forms. Presently, the quantity

$$dT = \frac{|A_l - A_v|}{\max(\mathrm{A_l}, \mathrm{A_v})} \tag{5.1}$$

is used as an accuracy indicator of the transition rates for $E1$ and $E2$ transitions [103, 123].

Our procedure of a separate optimization for each group of levels in studying transition probabilities has the advantage that electron relaxation effects are automatically included to a large extent. The radial orbitals for each group of levels were not quite orthogonal with each other for which a transformation to a biorthonormal basis was applied as described in Sec. 2.7.

5.2 Results and discussion

In Table 5.1 we present the number of CSFs used in the atomic wave function expansion for different level groups for VV and CV correlations as a function of the size of the increasing active set labelled by the highest principle quantum number n of the orbitals in the set. This table manifests that the extent of computations increases significantly for non-dynamic correlations and CV correlations as compared to VV correlations between each layer of the active set expansion.

Table 5.1: Number of CSFs used in the atomic state function for different level groups as a function of the size of the increasing active set labelled by the highest principle quantum number n of the of orbitals in the set.

			VV					CV				
Parity	J	Level numbers	$n=3$	$n=4$	$n=5$	$n=6$	$n=7$	$n=3$	$n=4$	$n=5$	$n=6$	$n=7$
odd	1/2	1	189	611	1746	3595	6158	543	10861	38397	89246	162599
	3/2	1	321	1028	3008	6252	10760	907	20789	78673	189829	352482
even	1/2	6	245	3375	13887	31859	57291	560	10875	37727	87050	157881
	3/2	8	413	5823	24548	56705	102294	936	20624	76765	184471	341642
	5/2	8	479	6850	29999	70038	126967	1051	25203	98846	245878	463036
	7/2	5	421	6415	29849	70819	129325	909	23217	94644	243368	465283
	9/2	2	313	5066	25511	61758	113807	648	17908	75284	200214	388242

In Table 5.2 we present the computed energies in Ni XII as a function of the increasing active set labelled by the n value of the orbitals in the set for both VV and CV correlations. Here the excitation energies are given relative to the $3s^23p^5$ $J = 3/2$ ground state and, as usual, we have assigned a level number in ascending order of the energy of each level, which is used in transition data tables to denote the individual transitions. Table 5.2 shows that the calculations are well converged with respect to increasing orbital set and our calculation set for CV correlations shows a more consistent convergence pattern for excitation energies with respect to an increasing size of the active space than VV correlations. It is obvious that the uncertainties cannot be further decreased by extending the orbital set to further layer of $n = 8$. Furthermore, we have found that the RCI calculations for each layer of calculations have reasonable effects on energy levels which is for layer $n = 7$ about 500 - 1500 cm^{-1} for all levels. So, the Breit interaction and leading QED effects that are included in RCI computations are important along with MCDHF calculations for the exact prediction of energy levels.

In Table 5.3, we present a detail comparison of our theoretical energy values from the layer $n = 7$. For this purpose we have taken four datasets available in the literature. Firstly, we compare with the *ab initio* values of [124] because they have used a larger configuration space than previous *ab initio* computations [125, 126]. Secondly, theoretical values from the CHIANTI V.8 [127, 128] because these are considered the most appropriate data for astrophysical applications [11]. Thirdly, with the most recent semi-empirically predicted and tentative experimental data values of [54]. Fourthly, with the NIST database [88] which is considered as the most criti-

Table 5.2: Excitation energies in cm^{-1} for NiXII as a function of the size of the increasing active set labelled by the highest principle quantum number n of the of orbitals in the set for valence-valence (VV) and core-valence (CV) correlations.

		MCDHF + RCI											
		VV						CV					
Level	*LSJ*	MR	$n = 3$	$n = 4$	$n = 5$	$n = 6$	$n = 7$	MR	$n = 3$	$n = 4$	$n = 5$	$n = 6$	$n = 7$
1	$^2P^o_{3/2}$	0	0	0	0	0	0	0	0	0	0	0	0
2	$^2P^o_{1/2}$	23 939	23 568	23 585	23 590	23 593	23 593	23 582	23 576	23 581	23 578	23 578	23 578
3	$^2S_{1/2}$	327 187	338 663	338 664	338 222	338 120	338 060	347 164	339 256	340 108	340 134	340 178	340 165
4	$^4D_{5/2}$	440 190	453 470	450 656	449 656	449 504	449 446	467 903	455 139	452 301	451 256	451 168	451 136
5	$^4D_{7/2}$	440 563	453 832	451 034	450 140	449 999	449 944	468 400	455 503	452 710	451 768	451 699	451 669
6	$^4D_{3/2}$	442 038	455 250	452 160	451 356	451 237	451 189	469 623	456 919	453 831	452 949	452 884	452 859
7	$^4D_{1/2}$	444 702	457 689	454 714	453 939	453 828	453 783	472 158	459 359	456 361	455 532	455 480	455 462
8	$^4F_{9/2}$	473 266	488 323	483 719	482 350	482 188	482 131	503 621	490 078	485 490	483 980	483 681	483 619
9	$^2P_{1/2}$	480 888	491 866	487 193	485 963	485 764	485 688	504 615	493 389	488 464	487 111	486 821	486 750
10	$^4F_{7/2}$	482 353	496 422	491 568	489 753	489 517	489 431	510 747	498 129	493 141	491 205	490 797	490 702
11	$^4F_{5/2}$	487 048	502 632	497 922	496 109	495 880	495 796	515 917	504 343	499 488	497 550	497 171	497 084
12	$^2P_{3/2}$	488 925	503 145	498 246	496 842	496 644	496 569	517 109	504 700	499 586	498 078	497 764	497 687
13	$^4F_{3/2}$	493 146	504 000	499 042	497 649	497 472	497 402	518 545	505 666	500 606	498 981	498 658	498 582
14	$^4P_{1/2}$	496 500	509 315	504 528	502 826	502 590	502 506	520 505	510 800	505 797	503 908	503 509	503 410
15	$^2D_{3/2}$	497 475	509 679	505 288	503 327	503 053	502 958	522 915	511 293	506 710	504 653	504 234	504 130
16	$^2F_{7/2}$	504 525	517 807	512 519	510 405	510 116	510 018	529 503	519 309	513 970	511 726	511 146	511 020
17	$^4P_{3/2}$	505 879	518 317	513 350	511 471	511 189	511 090	531 856	519 986	514 584	512 559	512 144	512 040
18	$^4P_{5/2}$	507 307	519 571	515 045	513 153	512 882	512 786	531 874	521 122	516 402	514 366	513 935	513 822
19	$^2D_{5/2}$	511 745	523 677	519 097	517 247	516 984	516 890	536 084	525 218	520 440	518 457	518 045	517 939
20	$^2G_{7/2}$	518 311	532 141	526 684	524 615	524 323	524 220	547 995	533 955	528 384	525 966	525 377	525 245
21	$^2G_{9/2}$	518 983	532 781	526 906	524 672	524 431	524 349	549 046	534 494	528 449	526 319	525 820	525 709
22	$^2F_{5/2}$	524 678	537 249	531 159	529 112	528 818	528 719	549 861	538 855	532 467	530 244	529 622	529 495
23	$^2F_{5/2}$	557 154	568 527	561 888	559 224	558 839	558 717	580 982	570 009	562 976	560 121	559 303	559 122
24	$^2F_{7/2}$	563 233	574 778	568 047	565 391	565 000	564 876	587 151	576 259	569 166	566 322	565 497	565 313
25	$^2D_{3/2}$	598 568	602 820	596 264	593 922	593 547	593 427	622 659	604 423	597 492	594 900	594 089	593 916
26	$^2D_{5/2}$	606 160	610 180	604 092	601 553	601 146	601 016	630 360	611 821	605 364	602 639	601 838	601 665
27	$^2S_{1/2}$	657 250	634 348	632 797	629 528	629 236	629 126	653 783	633 828	632 123	628 866	628 243	628 098
28	$^2P_{3/2}$	663 659	667 496	658 243	654 681	654 232	654 066	698 145	668 205	658 684	654 997	653 955	653 717
29	$^2P_{1/2}$	672 688	674 263	667 066	663 430	662 959	662 785	704 297	675 057	667 554	663 823	662 788	662 544
30	$^2D_{5/2}$	680 766	676 580	667 587	663 729	663 295	663 146	707 379	677 266	668 048	664 103	663 038	662 816
31	$^2D_{3/2}$	701 073	694 460	687 672	683 891	683 462	683 316	725 233	695 277	688 176	684 308	683 279	683 070

cally analysed database. Comparison with observed energies [54] and with the NIST values shows that the present *ab initio* values are not fully converged to experimental values. In order to achieve better accuracy relative to experimental values, we suggest more balanced and extended reference configuration sets as a starting point of the orbital expansion. This, however, results in very large expansions of wave functions which is computationally very expensive. Nevertheless, with the present set of calculations for CV correlations, results for the lowest 31 levels are better than obtained before in any *ab initio* investigation. A very good agreement with experiment is achieved to an accuracy better than 0.5% for low lying levels and 0.8% for higher lying levels whereas this accuracy is $1-2\%$ for the MCDF calculations of Fritzsche *et al.* [124] and for SUPERSTRUCTURE calculations available at CHIANTI V.8 [127, 128]. In some more detail, there is no experimental connection in NIST database to the 5 levels with $J = 7/2$ and two levels with $J = 9/2$ for the $3s^23p^43d$ configuration with other levels. The present results of energies for these 7 levels with less than 0.45% error with new tentative experimental assignments [54] testify them. However, we suggest different level ordering than provided by semi-empirical formalism of [54]. We briefly discuss later the shift in level ordering and reasons for it. We also note that there is 2100 cm^{-1} difference between the latest experimental energy [54] and NIST database for the level no. 31 ($^2D_{3/2}$). The present value of 683 070 cm^{-1} confirms the experimental energy [54] and we suggest a replacement in the NIST database with new experimental value.

Theoretically, level identification is always a difficult task because of the strong mixing of terms with same J and parity, whereas the mixing differs due to different set of configuration interaction and correlations. We provide LSJ mixing composition of terms for the 31 lowest states in Table 5.3. We found that our level ordering is same with SUPERSTRUCTURE calculations of Landi *et al.* [127] in the CHIANTI V.8 database for lowest order approximations and for the first correlation layer but they differ at two positions for our $n = 7$ correlation layer for the levels 16/17 ($^2F_{7/2}/^4P_{3/2}$) and 29/30 ($^2P_{1/2}/^2D_{5/2}$). Main reason for this could be the use of limited configuration interaction for their data set. Our level ordering as well as of Landi *et al.* differ from AUTOSTRUCTURE semi-empirical adjustments of Del Zanna and Badnell [54] at levels 8/9, 8 levels from level no. 11 to level no. 18 and then at levels 29/30. As many of the unknown levels are in this range, therefore, we have reason to believe that the term energy adjustments [55] in theoretical predictions of Del Zanna and Badnell [54] caused this level ordering difference. Additionally,

Table 5.3: Comparison of calculated and observed excitation energies in cm^{-1} for NiXII. Column 2 represents the LSJ mixing composition of terms for the 31 lowest states.

			MCDHF + RCI						
Level	Mixing	LSJ	E_{VV}	E_{CV}	E_{FR}	E_{CHI}	E_{DZ}	E_{obs}	E_{NIST}
1	96%	$^2P^o_{3/2}$	0	0	0	0	0	0	0
2	96%	$^2P^o_{1/2}$	23 593	23 578	23 560	23 049	24 444	23 629	23 629
3	71%+27(25%)	$^2S_{1/2}$	338 060	340 165		337 232	338 871	338 615	338 615
4	90%	$^4D_{5/2}$	449 446	451 136	450 740	453 155	449 645	452 755	
5	93%	$^4D_{7/2}$	449 944	451 669		453 827	450 723	454 036	454 000
6	89%	$^4D_{3/2}$	451 189	452 859	452 670	454 795	451 114		
7	90%	$^4D_{1/2}$	453 783	455 462	455 210	457 349	453 828		
8	90%	$^4F_{9/2}$	482 131	483 619		488 305	483 901	485 570	485 570
9	47%+29(40%)	$^2P_{1/2}$	485 688	486 750	488 970	490 909	482 248		
10	80%	$^4F_{7/2}$	489 431	490 702		495 355	490 839	492 790	492 750
11	93%	$^4F_{5/2}$	495 796	497 084	499 320	501 454	497 668	495 000	
12	30%+13(22%)+28 (22%)+17(13%)	$^2P_{3/2}$	496 569	497 687	500 080	501 956	493 404		
13	50%+12(12%)	$^4F_{3/2}$	497 402	498 582	500 930	502 613	501 278		
14	93%	$^4P_{1/2}$	502 506	503 410	506 230	507 833	496 677		
15	36%+31(21%)+13(18%)+6(11%)	$^2D_{3/2}$	502 958	504 130	506 710	508 170	496 904		
16	46%+20(26%)+10(12%)	$^2F_{7/2}$	510 018	511 020		516 799	510 921	513 322	513 290
17	66%+28(10%)	$^4P_{3/2}$	511 090	512 040	514 830	516 378	506 890	504 300	
18	59%+19(12%)+30(11%)	$^4P_{5/2}$	512 786	513 822	516 410	518 123	508 755		
19	37%+ 18(33%)+30(16%)	$^2D_{5/2}$	516 890	517 939	520 480	522 027	513 520	517 550	
20	62%+16(24%)	$^2G_{7/2}$	524 220	525 245		530 872	526 763	527 000	526 960
21	90%	$^2G_{9/2}$	524 349	525 709		531 064	528 177	527 270	527 230
22	67%+23(22%)	$^2F_{5/2}$	528 719	529 495	533 730	535 503	529 036	528 370	
23	73%+22(18%)	$^2F_{5/2}$	558 717	559 122	564 760	565 931	558 016		
24	76%+16(18%)	$^2F_{7/2}$	564 876	565 313		572 053	564 871	567 200	567 200
25	65%+15(24%)	$^2D_{3/2}$	593 427	593 916	599 510	599 556	594 911		
26	72%+19(15%)	$^2D_{5/2}$	601 016	601 665	606 830	606 915	603 754		
27	69%+3(23%)	$^2S_{1/2}$	629 126	628 098	633 710	630 076	622 917	622 836	622 840
28	49%+12(39%)	$^2P_{3/2}$	654 066	653 717	662 270	662 012	648 743	648 630	648 670
29	50%+9(43%)	$^2P_{1/2}$	662 785	662 544	671 000	671 182	658 765	657 360	657 290
30	65%+19(20%)	$^2D_{5/2}$	663 146	662 816	670 410	669 350	656 530	657 240	657 230
31	59%+15(15%)+25(13%)	$^2D_{3/2}$	683 316	683 070	690 500	689 361	678 384	678 520	676 420

FR: Theoretical energies of [124]
DZ: Semi empirically adjusted theoretical energies of [54]
obs: Experimental energies of [54]
CHI: Theoretical energies of CHIANTI V.8 [127, 128]
VV: Present calculation with valence-valence correlations
CV: Present calculation including core-valence correlations
NIST: [88]

there seems to be a problem with the tentative experimental energy assignment to the term $^4P_{3/2}$, which is level no 17 in our predictions. Del Zanna and Badnell [54] assigned an experimental value of 504 300 cm^{-1} to this level whereas present value of 512 040 cm^{-1}, [124] value of 514 830 cm^{-1} and [127] value of 516 378 cm^{-1} do not confirm this assignment. Moreover, there is no data available for the $^4P_{3/2}$ term in NIST database.

In the Table 5.4 we present our transition data in the region 146 − 316(Å) which is associated to $E1$ and $M2$ transitions from states of $3s3p^6$ and $3s^23p^43d$ to ground state $3s^23p^5$ levels. We have found that our calculations CV model are more stable in terms of accuracy between length and velocity form of $E1$ and $E2$ transitions. Here we present the data only in length form and used the velocity form in the estimation of the discrepancy of the two forms as given in Eq. 5.1. The lower values of dT do not represent an uncertainty estimate for each individual transition, but the average deviation within a given set of transitions, certainly provide inside into quality of the approximation. dT values of our results show a strong agreement between length and velocity gauge for all allowed strong transitions except for one weak intercombination transition from $^4D_{3/2} \rightarrow {}^2P^o_{1/2}$.

Table 5.4: $E1$ and $M2$ transition energies cm^{-1}, transition wavelengths λ in Å, transition rates A (s^{-1}) and weighted oscillator strengths (gf) for the $3s^23p^5 - 3s3p^6$ and $3s^23p^5 - 3s^23p^43d$ lines of NiXII. Level number of lower and upper level refer to Table 5.3. gf and A (s^{-1}) values are displayed in length gauge only. Column 7 is uncertainty estimator dT among the $E1$ transition between length and velocity gauge which is given in Eq. (5.1). The notation $x \pm n$ represents $x \times 10^n$.

Trans	Type	ΔE (cm^{-1})	λ (Å)	A (s^{-1})	gf	dT
31 - 1	$E1$	683070	146.398	6.595+09	8.476-02	0.013
30 - 1	$E1$	662816	150.871	2.144+11	4.390+00	0.008
29 - 1	$E1$	662543	150.933	3.988+10	2.724-01	0.003
31 - 2	$E1$	659492	151.632	2.029+11	2.798+00	0.008
28 - 1	$M2$	653717	152.971	1.185+02	1.663-09	
28 - 1	$E1$	653717	152.971	1.771+11	2.485+00	0.005
29 - 2	$E1$	638965	156.503	1.343+11	9.864-01	0.005
28 - 2	$E1$	630139	158.695	2.703+09	4.082-02	0.006
27 - 1	$E1$	628098	159.211	1.556+11	1.183+00	0.008
27 - 1	$M2$	628098	159.211	1.644+01	1.249-10	
27 - 2	$E1$	604520	165.420	4.152+10	3.406-01	0.011
26 - 1	$E1$	601664	166.206	3.100+08	7.703-03	0.011
26 - 1	$M2$	601664	166.206	3.484+01	8.657-10	
25 - 1	$E1$	593916	168.374	1.296+09	2.204-02	0.001
25 - 1	$M2$	593916	168.374	3.070+01	5.220-10	
25 - 2	$E1$	570338	175.335	8.423+08	1.553-02	0.022
25 - 2	$M2$	570338	175.335	1.745+01	3.217-10	

Table 5.4: (continued)

Trans	Type	ΔE (cm^{-1})	λ (Å)	A (s^{-1})	gf	dT
23 - 1	$E1$	559122	178.852	3.194+08	9.191-03	0.019
22 - 1	$E1$	529494	188.859	5.644+07	1.811-03	0.001
20 - 1	$M2$	525245	190.387	1.540+01	6.693-10	
19 - 1	$E1$	517939	193.073	1.088+08	3.649-03	0.008
18 - 1	$E1$	513822	194.620	1.656+08	5.643-03	0.007
18 - 1	$M2$	513822	194.620	8.318+01	2.834-09	
17 - 1	$E1$	512039	195.297	9.939+06	2.273-04	0.089
16 - 1	$M2$	511020	195.687	1.417+01	6.508-10	
22 - 2	$M2$	505916	197.661	1.540+01	5.412-10	
15 - 1	$E1$	504129	198.362	4.047+08	9.549-03	0.010
15 - 1	$M2$	504129	198.362	4.188+01	9.882-10	
14 - 1	$E1$	503409	198.645	6.358+08	7.523-03	0.015
14 - 1	$M2$	503409	198.645	2.723+01	3.222-10	
13 - 1	$E1$	498581	200.569	9.591+07	2.314-03	0.012
12 - 1	$M2$	497687	200.929	1.524+01	3.689-10	
12 - 1	$E1$	497687	200.929	3.035+08	7.349-03	0.016
11 - 1	$E1$	497084	201.173	1.059+08	3.856-03	0.016
19 - 2	$M2$	494361	202.281	1.265+02	4.657-09	
18 - 2	$M2$	490244	203.980	1.207+01	4.516-10	
17 - 2	$E1$	488461	204.724	5.443+06	1.368-04	0.030
17 - 2	$M2$	488461	204.724	1.088+02	2.734-09	
9 - 1	$M2$	486749	205.444	1.392+02	1.761-09	
9 - 1	$E1$	486749	205.444	3.274+07	4.143-04	0.045
15 - 2	$E1$	480551	208.094	1.636+08	4.248-03	0.000
14 - 2	$E1$	479831	208.406	9.367+07	1.220-03	0.008
13 - 2	$E1$	475003	210.525	1.666+07	4.429-04	0.063
12 - 2	$E1$	474109	210.922	1.420+08	3.790-03	0.001
12 - 2	$M2$	474109	210.922	1.823+01	4.863-10	
9 - 2	$E1$	463171	215.903	2.113+08	2.954-03	0.022
7 - 1	$M2$	455461	219.557	1.619+01	2.340-10	
7 - 1	$E1$	455461	219.557	9.548+06	1.380-04	0.000
6 - 1	$E1$	452859	220.819	1.194+07	3.492-04	0.007

Table 5.4: (continued)

Trans	Type	ΔE (cm^{-1})	λ (Å)	A (s^{-1})	gf	dT
5 - 1	$M2$	451668	221.401	9.496+01	5.583-09	
4 - 1	$E1$	451136	221.663	1.045+07	4.617-04	0.010
7 - 2	$E1$	431884	231.544	1.092+07	1.756-04	0.008
6 - 2	$E1$	429281	232.947	8.241+04	2.682-06	0.282
4 - 2	$M2$	427558	233.886	1.363+01	6.704-10	
3 - 1	$E1$	340164	293.975	4.128+09	1.070-01	0.019
3 - 1	$M2$	340164	293.975	5.326+01	1.380-09	
3 - 2	$E1$	316586	315.869	1.753+09	5.243-02	0.013

In Table 5.5, a brief comparison of our *ab initio* transition data are made with semi-empirical predictions for the $E1$ transitions from the states of $3s3p^6$ and $3s^23p^43d$ to the ground states of $3s^23p^5$ configuration. Generally, our results of strong transitions agree very well with the semi-empirical calculations of Del Zanna and Badnell [54] with less than 5% for most of the transitions, however, they differ more than 20% for a few weak $E1$ transitions. While our results for most of $E1$ transitions are in the range of 15% with the CHIANTI V.8 [127, 128] database. Above all, our systematically enlarged wave functions in present case should be flexible enough to include the important correlations and provide clearly improved data for all intercombination and intra-combination transitions.

A brief comparison of our $M1$ transition probabilities and transition wavelengths for a few intra-combination transitions is given in Table 5.6. This comparison shows that our $M1$ transition rates are in very good agreement with semi-empirical adjusted values of CHIANTI V.8 [127, 128] and with Del Zanna and Badnell [54]. Moreover, our transition wavelengths for several $M1$ transitions are better than the semi-empirical predictions of [54]. Overall, our predicted wavelengths for strong transitions deviate on the order of 0.8% while they excellently match for forbidden transition within the range of 1% deviation. From the comparison in Table 5.5 and 5.6 and by considering the agreement of our results from different gauges, we estimate the transition probabilities for all strong $E1$ lines to be accurate within $5-10$ per cent and for weak and forbidden transitions an accurate within $5-15$ per cent.

We calculated the radiative lifetime τ of each excited level j from our calculated

Table 5.5: Comparison of $E1$ weighted oscillator strengths (gf), transition rates A (s^{-1}) with previous predictions. Notations are the same as in Table 5.4.

Trans	Type	gf_{P}	gf_{CHI}	A_{P}	A_{CHI}	A_{DZ}
25 - 1	$E1$	2.20-02	2.125-02	1.30+09	1.274+09	1.04+09
25 - 2	$E1$	1.55-02	1.058-02	8.42+08	5.853+08	1.63+09
23 - 1	$E1$	9.19-03	7.832-03	3.19+08	2.788+08	4.09+08
22 - 1	$E1$	1.81-03	1.531-03	5.64+07	4.880+07	2.97+07
19 - 1	$E1$	3.65-03	3.098-03	1.09+08	9.384+07	1.79+08
17 - 1	$E1$	2.27-04	4.681-04	9.94+06	2.081+07	4.23+07
15 - 1	$E1$	9.55-03	8.563-03	4.05+08	3.687+08	8.24+07
14 - 1	$E1$	7.52-03	6.683-03	6.36+08	5.748+08	6.43+08
13 - 1	$E1$	2.31-03	2.634-03	9.59+07	1.110+08	2.57+08
12 - 1	$E1$	7.35-03	8.794-03	3.04+08	3.695+08	3.65+08
11 - 1	$E1$	3.86-03	3.071-03	1.06+08	8.584+07	1.06+08
9 - 1	$E1$	4.14-04	8.104-04	3.27+07	6.513+07	2.51+07
15 - 2	$E1$	4.25-03	4.114-03	1.64+08	1.610+08	2.78+07
14 - 2	$E1$	1.22-03	1.371-03	9.37+07	1.072+08	1.00+08
13 - 2	$E1$	4.43-04	1.049-03	1.67+07	4.012+07	1.42+08
12 - 2	$E1$	3.79-03	3.640-03	1.42+08	1.389+08	1.11+08
9 - 2	$E1$	2.95-03	3.765-03	2.11+08	2.742+08	1.62+08
7 - 1	$E1$	1.38-04	1.498-04	9.55+06	1.045+07	1.22+07
6 - 1	$E1$	3.49-04	3.318-04	1.19+07	1.144+07	1.24+07
4 - 1	$E1$	4.62-04	3.191-04	1.05+07	7.285+06	8.47+06
7 - 2	$E1$	1.76-04	1.765-04	1.09+07	1.107+07	1.22+07
3 - 1	$E1$	1.07-01	1.129-01	4.13+09	4.319+09	5.10+09
3 - 2	$E1$	5.24-02	5.621-02	1.75+09	1.860+09	2.17+09

CHI: Theoretical values of CHIANTI V.8 [127, 128]

P: Present calculation including core-valence correlations

DZ: Semi-empirically adjusted theoretical values of [54]

Table 5.6: Selection of $M1$ transition rates A (s^{-1}), weighted oscillator strengths (gf) and wavelengths λ in Å. Complete table for present $M1$ and $E2$ transition energies, transition rates, oscillator strengths and transition wavelengths is available online version of this article. Notations are the same as in Table 5.4.

Trans	J_F	J_I	Type	A_{P}	A_{CHI}	A_{DZ}	gf_{P}	λ_{P}	λ_{CHI}	λ_{DZ}	λ_{obs}
8 - 5	9/2	7/2	$M1$	2.45+01	2.111+01	2.80+01	3.59-07	3129.913	3167.570	3014.08	3171.18
21 - 8	9/2	9/2	$M1$	1.69+02	1.538+02	2.00+02	1.43-06	2375.826	2400.388	2258.57	2398.08
2 - 1	1/2	3/2	$M1$	2.35+02	2.373+02	2.60+02	1.27-06	4241.258	4232.096	4091.00	4232.09
16 - 5	7/2	7/2	$M1$	7.53+01	6.029+01	9.00+01	2.56-07	1684.884	1686.628	1661.20	1686.74
10 - 5	7/2	7/2	$M1$	1.72+01	1.599+01	1.80+01	1.35-07	2561.926	2580.650	2492.77	2580.38
16 - 8	7/2	9/2	$M1$	4.35+01	3.835+01	5.70+01	6.94-07	3649.437	3607.510	3701.00	3603.34
20 - 10	7/2	7/2	$M1$	6.29+01	5.246+01	8.40+01	6.32-07	2894.917	2923.127	2787.15	2923.12
24 - 8	7/2	9/2	$M1$	2.10+02	1.979+02	2.30+02	3.77-07	1224.073	1225.042	1235.02	1225.05

P: Present calculation including core-valence correlations
CHI: Theoretical values of CHIANTI V.8 [127, 128]
DZ: Theoretical values of [54]
obs: Experimental values of [54]

transition rates from the $n = 7$ computations using the following expression

$$\tau_j = \frac{1}{\sum_i A_{ji}}$$

and these are given in Table 5.7. These lifetimes of 30 excited states were calculated by including $E1$ and $E2$ transition rates in both length and velocity form as well as contributions from $M1$ and $M2$ transition rates. The average relative difference between length and velocity form is less than 4% for VV correlation whereas this difference is only 0.08% for the model including CV correlations. So our results with CV correlation are highly satisfactory in terms of computational consistency. There is a good agreement between theory and experiment for the first excited state ${}^2P^o_{1/2}$ which decays to ground state ${}^2P^o_{3/2}$ mainly by an $M1$ transition. The present value of 4.25 ms corroborates the semi-empirical value of 4.21 ms of the CHIANTI V.8 [127, 128] and benchmarks to the experimental value of 4.166±0.060 ms which was performed at the heavy ion storage ring at Max Plank Institute for Nuclear Physics Heidelberg, Germany [96]. However, the 3.85 ms value of Del Zanna and Badnell [54] does not come in the range of experimental uncertainty. The next excited level is the ${}^2S_{1/2}$ of the $3s3p^6$ configuration which has two decay branches caused mainly by allowed $E1$ transition to the two ground state terms. The present value of 173 ps for this state is better than the 162 ps of CHIANTI V.8 [127, 128] and 138 ps of Del Zanna and Badnell [54] compared to the experimental value of (190±10) ps [129], whereas other theories with value of 273 ps [125], 129.8 ps [126]

Table 5.7: Lifetimes (τ) in s for the low-lying levels of $3s^23p^5$, $3s3p^6$ and $3s^23p^43d$ are given in both length (τ_l) and velocity (τ_v) guage including $E1$, $M1$, $E2$ and $M2$ transitions among lowest 31 levels. Notations are the same as in Table 5.4.

	Level	τ_l	τ_v	τ_{CHI}	τ_{DZ}	τ_{obs}
1	$^2P^o_{3/2}$					
2	$^2P^o_{1/2}$	4.25-03	4.25-03	4.21-03	3.85-03	(4.166±0.060)-03[a]
3	$^2S_{1/2}$	1.70-10	1.73-10	1.62-10	1.38-10	(1.90±0.10)-10[b]
4	$^4D_{5/2}$	9.57-08	9.48-08			
5	$^4D_{7/2}$	1.05-02	1.05-02			
6	$^4D_{3/2}$	8.32-08	8.27-08			
7	$^4D_{1/2}$	4.88-08	4.91-08			
8	$^4F_{9/2}$	4.09-02	4.09-02			
9	$^2P_{1/2}$	4.10-09	4.20-09			
10	$^4F_{7/2}$	2.57-02	2.57-02			
11	$^4F_{5/2}$	9.44-09	9.29-09	1.16-08	9.43-09	(1.6±0.2)-08[c]
12	$^2P_{3/2}$	2.24-09	2.27-09			
13	$^4F_{3/2}$	8.88-09	9.06-09	6.62-09	2.51-09	(2.0±0.2)-08[c]
14	$^4P_{1/2}$	1.37-09	1.35-09			
15	$^2D_{3/2}$	1.76-09	1.75-09			
16	$^2F_{7/2}$	5.68-03	5.68-03			
17	$^4P_{3/2}$	6.50-08	6.82-08	4.37-08	1.77-08	(2.0±0.2)-08[c]
18	$^4P_{5/2}$	6.04-09	5.99-09			
19	$^2D_{5/2}$	9.19-09	9.26-09	1.07-08	5.59-09	(8.2±1.0)-09[c]
20	$^2G_{7/2}$	5.16-03	5.16-03			
21	$^2G_{9/2}$	4.73-03	4.73-03			
22	$^2F_{5/2}$	1.77-08	1.77-08	2.05-08	3.37-08	(1.5±0.15)-08[c]
23	$^2F_{5/2}$	3.13-09	3.07-09			
24	$^2F_{7/2}$	1.90-03	1.90-03			
25	$^2D_{3/2}$	4.68-10	4.63-10			
26	$^2D_{5/2}$	3.23-09	3.26-09			
27	$^2S_{1/2}$	5.07-12	5.03-12			
28	$^2P_{3/2}$	5.56-12	5.53-12			
29	$^2P_{1/2}$	5.74-12	5.71-12			
30	$^2D_{5/2}$	4.66-12	4.63-12			
31	$^2D_{3/2}$	4.77-12	4.73-12			

a : Experimental values form [96]
b : Experimental values form [129]
c : Experimental values form [51]
CHI: Theoretical values of CHIANTI V.8 [127, 128]
DZ: Theoretical values of [54]

as well as semi-empirical value of 238 ps [130] predicted a much scattered lifetime for this state.

As far as next 28 higher states arising from the $3s^23p^43d$ are concerned, only few experimental lifetimes are available and these are mainly based on beam foil spectroscopy [51]. As already discussed, the correlation effects for Ni XII like complex are rather large. So, 10% deviation from the theory is highly acceptable [129] for lifetimes. On the other hand lifetimes from the beam foil spectroscopy for many electron systems suffer from Doppler shift problems for the shorter lifetimes and from the cascade re-population for the longer lifetimes [11]. Nevertheless, the present lifetimes for the five levels have good agreement with the experiment. More specifically, the present lifetimes for level no. 19 ($^2D_{5/2}$) and 22 ($^2F_{5/2}$) are better than semi-empirical predictions. Although, the present lifetime for the level no. 13 ($^4F_{3/2}$) is better than semi-empirical values but it differs by a factor of two with the experiment. The CHIANTI V.8 [127, 128] and Del Zanna and Badnell [54] lifetime value for the level no. 17 ($^4P_{3/2}$) is better than the present value. For the level no. 11 ($^4F_{5/2}$) the lifetime of the CHIANTI V.8 [127, 128] is in very good agreement with experiment, however, the present value as well as value of Del Zanna and Badnell [54] matches with each other but differs by a factor of two with the experiment. Overall, from the comparison of length and velocity gauges and with the agreement with experiment and semi-empirical formalisms, we are confident that the present lifetime dataset will corroborate the future beam foil measurements and electron beam ion trap measurements with better quality than the semi-empirical formalism in a similar manner as the previous prediction for such ions [131–133].

6 Summary

In this thesis, we have presented high-precision calculations for rates and line strengths in various many-electron atomic systems in the view of high precision experiments. We started this thesis with a brief introduction in Chapter 1. In Chapter 2, we have demonstrated how the MCDHF wave functions for many-electron atomic systems are improved including the correlation, Breit, first order QED and finite nuclear mass corrections. Then we have shown how these wave functions are used to calculate the transition amplitudes necessary for the calculation of transition properties of different multi-pole expansions of the electromagnetic field.

In Chapter 3, we have presented highly accurate calculations for the line strengths of QED-sensitive forbidden transitions. We have extended the high precision evaluations previously performed for the middle Z B-like ions to higher Z as well as to different systems such as F-, Al-, and Cl- like ions. The obtained line strengths are further improved by rigorous calculations of the QED correction within an extended Furry picture approach. We used up-to-date accurate transition energies for the calculations of the $M1$ transition rates and reported lifetimes in the millisecond to picoseconds range. We believe that our accurate theoretical predictions provide the prerequisite for a test of QED by lifetime measurements at different frequencies and timescales. This will help to find a reason for the present discrepancies between theory and experiment for B-like Ar and Al-like Fe. Apart from testing atomic structure theory, such experiments in the future agreeing with the theoretical investigations will be very helpful for terrestrial and astrophysical plasma diagnostics.

In Chapter 4, we have presented high precision atomic calculations of the line strength of the $1s^22s2p\ ^1P_1\ -\ 1s^22s^2\ ^1S_0$ spin allowed $E1$ transition in Be-like carbon. For the wave functions of the excited and ground state, we incorporated higher-order electron correlations, where the orbital relaxation and overlaps were taken into account by using separate and simultaneous set of relativistic orbitals in the active set. This has helped us to reliably estimate the uncertainty of the obtained line strength. Moreover, the finite nuclear mass correction to the line strength is calculated by correcting the energy, wave functions as well as the transition operator. The achieved relative uncertainty of the line strength amounts to

10^{-4}, which represents a reliable theoretical benchmark of $E1$ line strength in a view of upcoming high precision lifetime measurement of the $1s^2 2s2p\ ^1P_1$ state of Be-like carbon. Extensions of current studies to heavier Be-like ions allow us to improve the theoretical accuracy of transition rates. The given (numerical) uncertainty together with the high precision experiments will allow an alternative spectroscopic test than the energy alone and will provide further insight into the atomic structure of many-electrons atoms and ions.

Finally, in Chapter 5, We have presented calculations for the $E1, E2, M1$ and $M2$ transitions between $n = 3 \rightarrow 3$ states of Ni XII complex and critically compared it to other theories and experiment. We have achieved good numerical convergence for the desired parameters with our substantially extended computations comprising over two million CSFs. By incorporating all important relativistic and correlation contributions, we have achieved the same level of accuracy as semi-empirical calculations for observed transitions. We have justified the recently identified lines and suggested a level ordering for the first 31 levels based on the first principle. We have presented the pure *ab initio* lifetime values which are better than the values from the semi-empirical formalism as compared to the available experiments, therefore, we expect better accuracy than the semi-empirical tabulations for the upcoming experiments.

Bibliography

[1] X. Zhang and J. Ye. “Precision measurement and frequency metrology with ultracold atoms”. In: *National Science Review* 3 (2016), pp. 189–200.

[2] J. R. C. López-Urrutia. “Frequency metrology using highly charged ions”. In: *Journal of Physics: Conference Series* 723 (2016), p. 012052.

[3] S. Kraft-Bermuth et al. “Microcalorimeters for X-Ray Spectroscopy of Highly Charged Ions at Storage Rings”. In: *Atoms* 6 (2018), p. 040059.

[4] A. V. Volotka et al. “Progress in quantum electrodynamics theory of highly charged ions”. In: *Annalen der Physik* 525 (2013), pp. 636–646.

[5] V. M. Shabaev et al. “Stringent tests of QED using highly charged ions”. In: *Hyperfine Interactions* 239 (2018), p. 60.

[6] M. S. Safronova et al. “Search for new physics with atoms and molecules”. In: *Review of Modern Physics* 90 (2018), p. 025008.

[7] , familyi=c., given=I., giveni=I., „ et al. “High Precision Wavelength Measurements of QED-Sensitive Forbidden Transitions in Highly Charged Argon Ions”. In: *Physical Review Letters* 91 (2003), p. 183001.

[8] A. N. Artemyev et al. “QED Calculation of the $2p_{3/2}-2p_{1/2}$ Transition Energy in Boronlike Argon”. In: *Physical Review Letters* 98 (2007), p. 173004.

[9] V. Mäckel et al. “Laser Spectroscopy on Forbidden Transitions in Trapped Highly Charged Ar^{13+} Ions”. In: *Physical Review Letters* 107 (2011), p. 143002.

[10] A. N. Artemyev et al. “Ab initio calculations of the $2p_{3/2}-2p_{1/2}$ fine-structure splitting in boronlike ions”. In: *Physical Review A* 88 (2013), p. 032518.

[11] E. Träbert. “Critical Assessment of Theoretical Calculations of Atomic Structure and Transition Probabilities: An Experimenter’s View”. In: *Atoms* 2 (2014), pp. 15–85.

[12] E. Träbert. “In pursuit of highly accurate atomic lifetime measurements of multiply charged ions”. In: *Journal of Physics B: Atomic, Molecular and Optical Physics* 43 (2010), p. 074034.

[13] A. Lapierre et al. “Relativistic Electron Correlation, Quantum Electrodynamics, and the Lifetime of the $1s^2 2s^2 2p\ {}^2P^o_{3/2}$ Level in Boronlike Argon”. In: *Physical Review Letters* 95 (2005), p. 183001.

[14] G. Brenner et al. “Lifetime determination of the Fe *XIV* $3s^2 3p\,{}^2P^o_{3/2}$ metastable level”. In: *Physical Review A* 75 (2007), p. 032504.

[15] I. I. Tupitsyn et al. “Magnetic-dipole transition probabilities in B-like and Be-like ions”. In: *Physical Review A* 72 (2005), p. 062503.

[16] A. V. Volotka et al. “Radiative corrections to the magnetic-dipole transition amplitude in B-like ions”. In: *The European Physical Journal D - Atomic, Molecular, Optical and Plasma Physics* 38 (2006), pp. 293–298.

[17] A. V. Volotka et al. “Nuclear recoil effect on the magnetic-dipole decay rates of atomic levels”. In: *The European Physical Journal D* 48 (2008), pp. 167–170.

[18] P. Rynkun et al. “Energies and E1, M1, E2, M2 transition rates for states of the 2s22p, 2s2p2, and 2p3 configurations in boron-like ions between N III and Zn XXVI”. In: *Atomic Data and Nuclear Data Tables* 98 (2012), pp. 481 –556.

[19] J. Marques, P. Indelicato, and F. Parente. “Relativistic multiconfiguration calculations of the 2s22p 2P3/2 level lifetime along the boron isoelectronic sequence”. In: *The European Physical Journal D* 66 (2012), p. 324.

[20] C. F. Fischer et al. “Lifetimes of some $2s^2 2p^2 P_{3/2}$ states from variational theory”. In: *Physical Review A* 93 (2016), p. 022505.

[21] M. J. Vilkas and Y. Ishikawa. “Relativistic multireference many-body perturbation-theory calculations on the multiple openshell states in siliconlike Ar and aluminumlike Fe ions”. In: *Physical Review A* 68 (2003), p. 012503.

[22] J. A. Santana, Y. Ishikawa, and E. Träbert. “Multireference Møller–Plesset perturbation theory results on levels and transition rates in Al-like ions of iron group elements”. In: *Physica Scripta* 79 (2009), p. 065301.

[23] A. H. Zewail. “Femtochemistry - Atomic-Scale Dynamics of the Chemical Bond”. In: *The Journal of Physical Chemistry A* 104 (2000), pp. 5660–5694.

[24] J. F. Sell et al. “Lifetime measurement of the cesium $6P_{3/2}$ state using ultrafast laser-pulse excitation and ionization”. In: *Physical Review A* 84 (2011), p. 010501.

[25] B. M. Patterson et al. “Lifetime measurement of the cesium $6P_{3/2}$ level using ultrafast pump-probe laser pulses”. In: *Physical Review A* 91 (2015), p. 012506.

[26] E. Träbert. “Measurement of femtosecond atomic lifetimes using ion traps”. In: *Applied Physics B* 114 (2014), pp. 167–172.

[27] J. Rothhardt et al. “Lifetime measurements of ultra-short-lived excited states in Be-like ions”. In: *X-Ray Spectrometry* (In Press 2019).

[28] S. Demmler et al. “Generation of high photon flux coherent soft x-ray radiation with few-cycle pulses”. In: *Optics Letters* 38 (2013), pp. 5051–5054.

[29] J. Rothhardt et al. “Enhancing the Macroscopic Yield of Narrow-Band High-Order Harmonic Generation by Fano Resonances”. In: *Physical Review Letters* 112 (2014), p. 233002.

[30] C. F. Fischer. “Allowed transitions and intercombination lines in C III and C II”. In: *Physica Scripta* 49 (1994), pp. 323–330.

[31] A. Ynnerman and C. F. Fischer. “Multiconfigurational-Dirac-Fock calculation of the $2s^2\ {}^1S_0$–2s2p ${}^3P_1$ spin-forbidden transition for the Be-like isoelectronic sequence”. In: *Physical Review A* 51 (1995), pp. 2020–2030.

[32] P. Jönsson and C. Froese Fischer. “Multiconfiguration Dirac-Fock calculations of the $2s^{21}S_0 - -2s2p^3P_1$ intercombination transition in C III”. In: *Physical Review A* 57 (1998), pp. 4967–4970.

[33] K. Wang et al. “Benchmarking Atomic Data for Astrophysics: Be-like Ions between B ii and Ne vii”. In: *The Astrophysical Journal Supplement Series* 234 (2018), p. 40.

[34] U. I. Safronova et al. “Relativistic Many-Body Calculations of Transition Probabilities for the $2l_1 2l_2[LSJ]$–$2l_3 2l_4[L'S'J']$ Lines in Be-like Ions”. In: *Physica Scripta* 59 (1999), pp. 286–295.

[35] M. H. Chen, K. T. Cheng, and W. R. Johnson. “Large-scale relativistic configuration-interaction calculation of the $2s^{21}S_0 - 2s2p^3P_1$ intercombination transition in C III”. In: *Physical Review A* 64 (2001), p. 042507.

[36] I. M. Savukov. “Relativistic configuration-interaction perturbation-theory method with application to intercombination and allowed transitions of light Be-like ions”. In: *Physical Review A* 70 (2004), p. 042502.

[37] K. B. Fournier et al. Tokamak spectroscopy for X-ray astronomy, Proc. Workshop on Atomic Data Needs for X-ray Astronomy: NASA-CP-2000-209968, 127. Available at: http://heasarc.gsfc.nasa.gov/docs/heasarc/atomic. 2000.

[38] J. M. Miller et al. “The magnetic nature of disk accretion onto black holes”. In: *Nature* 441 (2006), pp. 953–955.

[39] T. R. Kallman et al. “Spectrum synthesis modeling of the X-Ray spectrum of GRO J1655-40 taken during the 2005 outburst”. In: *The Astrophysical Journal* 701 (2009), pp. 865–884.

[40] T. Tamura et al. “X-RAY Spectroscopy of the core of the Perseus cluster WITHSUZAKU: elemental abundances in the intracluster medium”. In: *The Astrophysical Journal* 705 (2009), pp. L62–L66.

[41] T. Tamagawa et al. AIP Conf. Proc. Vol. 1269, Origin of Matter and Evolution of Galaxies: OMEG-2010, Am. Inst. Phys., New York, 137. 2010.

[42] K. Koyama et al. ASP Conf. Ser. Vol. 439 The Galactic Center: A Window to the Nuclear Environment of Disk Galaxies. Astron. Soc. Pac., San Francisco. 2011.

[43] L. Malinovsky and M. Heroux. “An Analysis of the Solar Extreme-Ultraviolet Between 50 and 300 A”. In: *Astrophysical Journal* 181 (1973), pp. 1009–1030.

[44] A. J. J. Raassen et al. “High-resolution X-ray spectroscopy of Procyon by Chandra and XMM-Newton”. In: *Astronomy & Astrophysics* 389 (2002), pp. 228–238.

[45] A. H. Gabriel, B. C. Fawcett, and C. Jordan. “Classification of iron VIII to XII and XIV lines in the solar extreme ultra-violet spectrum and their isoelectronic sequences from argon to nickel”. In: *Proceedings of the Physical Society* 87 (1966), pp. 825–839.

[46] B. Edlén and R. Smitt. “The forbidden transitions within 3s2 3p5 3d of Fe ix and Ni xi and 3s2 3p4 3d of Fe x and Ni xii”. In: *Solar Physics* 57 (1978), pp. 329–339.

[47] A. Matthews et al. “Effective collision strengths for electron-impact excitation of Ni XII”. In: *Atomic Data and Nuclear Data Tables* 70 (1998), pp. 41 –61.

[48] E. Hinnov et al. “Long-wavelength magnetic dipole lines of highly ionized nickel measured in Tokamak Fusion Test Reactor plasmas”. In: *J. Opt. Soc. Am. B* 7 (1990), pp. 2002–2005.

[49] M Mattioli et al. “Experimental and simulated M-shell nickel spectra in the 14.4–18.0 nm region from magnetic fusion devices”. In: *Journal of Physics B: Atomic, Molecular and Optical Physics* 37 (2003), pp. 13–40.

[50] F. P. Keenan et al. “Extreme ultraviolet emission lines of Ni xii in laboratory and solar spectra”. In: *Monthly Notices of the Royal Astronomical Society* 318 (2000), pp. 37–39.

[51] E Trabert et al. “Beam-foil measurements on intercombination transitions in Cl-like ions of elements Mn through Zn”. In: *Physica Scripta* 48 (1993), pp. 580–585.

[52] L. Yang et al. “Effect of structure random disturbances on characterizations of microstructured optical fibres”. In: *Chinese Physics* 14 (2005), pp. 2235–2240.

[53] T. Shirai et al. “Spectral Data for Highly Ionized Atoms: Ti, V, Cr, Mn, Fe, Co, Ni, Cu, Kr, and Mo”. In: *Journal of Physical and Chemical Reference Data Monographs* 8 (2000), p. 360.

[54] G. D. Zanna and N. R. Badnell. “Atomic data for astrophysics: Ni XII”. In: *Astronomy & Astrophysics* 585 (2016), A118.

[55] H. Nussbaumer and P. J. Storey. “The C III transition probabilities”. In: *Astronomy & Astrophysics* 64 (1978), pp. 139–144.

[56] N. Badnell. “A Breit–Pauli distorted wave implementation for autostructure”. In: *Computer Physics Communications* 182 (2011), pp. 1528 –1535.

[57] Y. Ishikawa and M. J. Vilkas. “Relativistic many-body calculations of excited-state energies and transition wavelengths for six-valence-electron sulfurlike ions”. In: *Physical Review A* 78 (2008), p. 042501.

[58] C. Froese Fischer, B. T., and P. Jönsson. *Computational atomic structure : an MCHF approach.* Bristol, UK Philadelphia, Penn: Institute of Physics Publ, 1997.

[59] I. P. Grant. *Relativistic Quantum Theory of Atoms and Molecules: Theory and Computation.* Springer, New York, 2007.

[60] C. F. Fischer et al. “Advanced multiconfiguration methods for complex atoms: I. Energies and wave functions”. In: *Journal of Physics B: Atomic, Molecular and Optical Physics* 49 (2016), p. 182004.

[61] J. P. Desclaux. “A multiconfiguration relativistic DIRAC-FOCK program”. In: *Computer Physics Communications* 9 (1975), pp. 31 –45.

[62] I. P. Grant. “Relativistic atomic structure: past, present and future”. In: *Journal of Physics B: Atomic, Molecular and Optical Physics* 43 (2010), p. 074033.

[63] I. Grant et al. “An atomic multiconfigurational Dirac-Fock package”. In: *Computer Physics Communications* 21 (1980), pp. 207 –231.

[64] K. Dyall et al. “GRASP: A general-purpose relativistic atomic structure program”. In: *Computer Physics Communications* 55 (1989), pp. 425 –456.

[65] F. A. Parpia, C. F. Fischer, and I. P. Grant. “GRASP92: A package for large-scale relativistic atomic structure calculations”. In: *Computer Physics Communications* 94 (1996), pp. 249 –271.

[66] F. Parpia, C. F. Fischer, and I. Grant. “GRASP92: a package for large-scale relativistic atomic structure calculations”. In: *Computer Physics Communications* 175 (2006), pp. 745 –747.

[67] P. Jönsson et al. “The grasp2K relativistic atomic structure package”. In: *Computer Physics Communications* 177 (2007), pp. 597 –622.

[68] P. Jönsson et al. “New version: Grasp2K relativistic atomic structure package”. In: *Computer Physics Communications* 184 (2013), pp. 2197 –2203.

[69] C. F. Fischer et al. “GRASP2018—A Fortran 95 version of the General Relativistic Atomic Structure Package”. In: *Computer Physics Communications* 237 (2019), pp. 184 –187.

[70] I. P. Grant and N. C. Pyper. “Breit interaction in multi-configuration relativistic atomic calculations”. In: *Journal of Physics B: Atomic and Molecular Physics* 9 (1976), pp. 761–774.

[71] D. S. Hughes and C. Eckart. “The Effect of the Motion of the Nucleus on the Spectra of Li I and Li II”. In: *Physical Review* 36 (1930), pp. 694–698.

[72] I. I. Tupitsyn et al. “Relativistic calculations of isotope shifts in highly charged ions”. In: *Physical Review A* 68 (2003), p. 022511.

[73] W. Liu. *Handbook of relativistic quantum chemistry.* Berlin, Germany: Springer, 2016.

[74] J. Olsen et al. “Transition probability calculations for atoms using nonorthogonal orbitals”. In: *Phys. Rev. E* 52 (1995), pp. 4499–4508.

[75] M. Bilal et al. “Line strengths of QED-sensitive forbidden transitions in B-, Al-, F- and Cl-like ions”. In: *Physical Review A* 97 (2018), p. 052506.

[76] A. V. Volotka. “High-precision QED calculations of the hyperfine structure in hydrogen and transition rates in multicharged ions”. PhD thesis. Technische Universität Dresden, 2006.

[77] D. K. Nandy. “Relativistic coupled-cluster calculations of transition properties in highly charged inert-gas ions”. In: *Physical Review A* 94 (2016), p. 052507.

[78] P. Jönsson, A. Alkauskas, and G. Gaigalas. “Energies and E1, M1, E2 transition rates for states of the 2s22p5 and 2s2p6 configurations in fluorine-like ions between Si VI and W LXVI”. In: *Atomic Data and Nuclear Data Tables* 99 (2013), pp. 431 –446.

[79] V. Jonauskas, et al. “Relativistic allowed and forbidden transition probabilities for fluorine-like Fe XVIII*”. In: *Astronomy & Astrophysics* 416 (2004), pp. 383–389.

[80] K. M. Aggarwal and F. P. Keenan. “Radiative rates for E1, E2, M1, and M2 transitions in F-like ions with 37 - 53”. In: *Atomic Data and Nuclear Data Tables* 109-110 (2016), pp. 205 –338.

[81] K. M. Aggarwal and F. P. Keenan. “Radiative rates for E1, E2, M1, and M2 transitions in S-like to F-like tungsten ions (W LIX to W LXVI)”. In: *Atomic Data and Nuclear Data Tables* 111-112 (2016), pp. 187 –279.

[82] D. K. Nandy and B. K. Sahoo. “Spectral properties of a few F-like ions”. In: *Astronomy & Astrophysics* 563 (2014), A25.

[83] D. P. Moehs, M. I. Bhatti, and D. A. Church. “Measurements and calculations of metastable level lifetimes in FeX, FeXI, FeXII, FeXIII, and FeXIV”. In: *Physical Review A* 63 (2001), p. 032515.

[84] K. M. Aggarwal and F. P. Keenan. “Energy levels, radiative rates, and lifetimes for transitions in W LVIII”. In: *Atomic Data and Nuclear Data Tables* 100 (2014), pp. 1603 –1767.

[85] Y. Ishikawa, J. A. Santana, and E. Träbert. “Relativistic multireference many-body perturbation theory for open-shell ions with multiple valence shell electrons: the transition rates and lifetimes of the excited levels in chlorinelike Fe X”. In: *Journal of Physics B: Atomic, Molecular and Optical Physics* 43 (2010), p. 074022.

[86] G. Singh and N. K. Puri. “Revised and extended calculations of level energies, M1 and E2 radiative rates for highly charged tungsten ions from W^{57+} to W^{60+}”. In: *Journal of Physics B: Atomic, Molecular and Optical Physics* 49 (2016), p. 205002.

[87] H. Gharibnejad and A. Derevianko. “Coupled-cluster calculations of properties of the boron atom as a monovalent system”. In: *Physical Review A* 86 (2012), p. 022505.

[88] A. Kramida et al. NIST Atomic Spectra Database (ver. 5.6.1), [Online]. Available: `https://physics.nist.gov/asd` [2019, February 18]. National Institute of Standards and Technology, Gaithersburg, MD. 2018.

[89] F. G. Serpa, J. D. Gillaspy, and E Träbert. “Lifetime measurements in the ground configuration of and using an electron beam ion trap”. In: *Journal of Physics B: Atomic, Molecular and Optical Physics* 31 (1998), pp. 3345–3352.

[90] D. P. Moehs and D. A. Church. “Magnetic dipole transition rates from measured lifetimes of levels of Be-like and B-like argon ions”. In: *Physical Review A* 58 (1998), pp. 1111–1114.

[91] E. Träbert et al. “Experimental M1 Transition Rates of Coronal Lines from Arx, Arxiv, and Arxv”. In: *The Astrophysical Journal* 541 (2000), pp. 506–511.

[92] S. J. Smith, A. Chutjian, and J. A. Lozano. “Measurement of metastable lifetimes for transitions in Fe^{9+}, Fe^{10+}, and Fe^{13+}”. In: *Physical Review A* 72 (2005), p. 062504.

[93] P. Beiersdorfer, E. Trabert, and E. H. Pinnington. “Experimental Transition Rate of the Green Coronal Line of Fexiv”. In: *The Astrophysical Journal* 587 (2003), pp. 836–840.

[94] D. P. Moehs and D. A. Church. “Measured Level Lifetimes for the Coronal Transitions of Fe X and Fe XIV”. In: *The Astrophysical Journal* 516 (1999), pp. L111–L113.

[95] G. Brenner et al. “On the transition rate of the Fe X red coronal line”. In: *The Astrophysical Journal* 703 (2009), pp. 68–73.

[96] E Träbert, G Saathoff, and A Wolf. “M1/E2 decay rates in Co XI, Ni XII and Cu XIII measured at a heavy-ion storage ring”. In: *Journal of Physics B: Atomic, Molecular and Optical Physics* 37 (2004), pp. 945–952.

[97] S. W. Epp et al. “Soft X-Ray Laser Spectroscopy on Trapped Highly Charged Ions at FLASH”. In: *Physical Review Letters* 98 (2007), p. 183001.

[98] M. Bilal et al. “High precision calculations of the $1s^22s2p\ ^1P_1 - 1s^22s^2\ ^1S_0$ spin allowed $E1$”. In: *Submitted to Physical Review A* (2019).

[99] V. Hilbert et al. “A compact and turnkey narrow-bandwidth and high-photon-flux XUV source”. In: *Review of Scientific Instruments* (In preparation 2019).

[100] J Rothhardt et al. “Prospects for laser spectroscopy of highly charged ions with high-harmonic XUV and soft x-ray sources”. In: *Physica Scripta* T166 (2015), p. 014030.

[101] I. M. Savukov and W. R. Johnson. “Equality of length-form and velocity-form transition amplitudes in relativistic many-body perturbation theory”. In: *Physical Review A* 62 (2000), p. 052506.

[102] P. Indelicato, V. M. Shabaev, and A. V. Volotka. “Interelectronic-interaction effect on the transition probability in high-Z He-like ions”. In: *Physical Review A* 69 (2004), p. 062506.

[103] C. F. Fischer. “Evaluating the accuracy of theoretical transition data”. In: *Physica Scripta* T134 (2009), p. 014019.

[104] C. F. Fischer. “Towards accurate transition data for $3\mathrm{p}2, 3\mathrm{p}3, 3\mathrm{p}4$levels of Fe, Co and Ni ions”. In: *Journal of Physics B: Atomic, Molecular and Optical Physics* 43 (2010), p. 074020.

[105] J. Bieroń et al. “Ab initio calculations of the hyperfine structure of zinc and evaluation of the nuclear quadrupole moment $Q(^{67}\mathrm{Zn})$”. In: *Physical Review A* 97 (2018), p. 062505.

[106] L. Filippin et al. “Multiconfiguration calculations of electronic isotope shift factors in Al i”. In: *Physical Review A* 94 (2016), p. 062508.

[107] Z. Fried and A. D. Martin. "Center-of-mass effect on electromagnetic transition rates in mesic atoms". In: *Il Nuovo Cimento* 29 (1963), pp. 574–576.

[108] Z.-C. Yan and G. W. F. Drake. "Theoretical lithium 2^2S$\rightarrow$$2^2$P and 2^2P$\rightarrow$$3^2$D oscillator strengths". In: *Physical Review A* 52 (1995), R4316–R4319.

[109] S. G. Karshenboim. "Two-body effects in the decay rate of atomic levels". In: *Physical Review A* 56 (1997), pp. 4311–4313.

[110] Z.-C. Yan, M. Tambasco, and G. W. F. Drake. "Energies and oscillator strengths for lithiumlike ions". In: *Physical Review A* 57 (1998), pp. 1652–1661.

[111] W. Johnson, D. Plante, and J. Sapirstein. "Relativistic Calculations of Transition Amplitudes in the Helium Isoelectronic Sequence". In: ed. by B. Bederson and H. Walther. Vol. 35. Advances In Atomic, Molecular, and Optical Physics. Academic Press, 1995, pp. 255 –329.

[112] A. Derevianko et al. "Negative-energy contributions to transition amplitudes in heliumlike ions". In: *Physical Review A* 58 (1998), pp. 4453–4461.

[113] V. G. Ivanov and S. G. Karshenboim. "Radiative corrections to dipole matrix elements in hydrogen-like atoms". In: *Physics Letters A* 210 (1996), pp. 313 –316.

[114] J. Sapirstein, K. Pachucki, and K. T. Cheng. "Radiative corrections to one-photon decays of hydrogenic ions". In: *Physical Review A* 69 (2004), p. 022113.

[115] L. Heroux. "Radiative Lifetimes for uv Multiplets of C ii and C iii". In: *Phys. Rev.* 180 (1969), pp. 1–5.

[116] M. C. Poulizac and J. P. Buchet. "Beam-Foil Spectroscopy of Carbon in the Vacuum Ultraviolet". In: *Physica Scripta* 4 (1971), pp. 191–194.

[117] M. C. Buchet-Poulizac and J. P. Buchet. "Lifetime Measurements of Carbon in the Extreme Ultra-Violet". In: *Physica Scripta* 8 (1973), pp. 40–42.

[118] M.-W. Chang. "Mean lives of some astrophysically important excited levels in carbon, nitrogen, and oxygen". In: *The Astrophysical Journal* 211 (1977), p. 300.

[119] N Reistad et al. “Lifetimes of Levels in C II and C III, Derived from Beam-Foil Experiments and Extensive Cascade Analyses”. In: *Physica Scripta* 34 (1986), pp. 151–157.

[120] N. Reistad and I. Martinson. “Accurate transition probabilities in ions obtained by isoelectronic smoothing of line strengths”. In: *Physical Review A* 34 (1986), pp. 2632–2637.

[121] M. Bilal et al. “Ab initio calculations of energy levels, transition rates and lifetimes in Ni xii”. In: *Monthly Notices of the Royal Astronomical Society* 469 (2017), pp. 4620–4629.

[122] P. Jönsson et al. “Accurate multiconfiguration calculations of energy levels, lifetimes, and transition rates for the silicon isoelectronic sequence”. In: *Astronomy & Astrophysics* 585 (2016), A26.

[123] J. Ekman, M. Godefroid, and H. Hartman. “Validation and Implementation of Uncertainty Estimates of Calculated Transition Rates”. In: *Atoms* 2 (2014), pp. 215–224.

[124] S Fritzsche et al. “Level energies and lifetimes in the 3p43dconfiguration of chlorine-like ions”. In: *Physica Scripta* 52 (1995), pp. 258–266.

[125] M. Vajed-Samii and K. MacDonald. “Electric dipole transitions in Cl-like ions”. In: *Atomic Data and Nuclear Data Tables* 26 (1981), pp. 467 –475.

[126] K.-N. Huang et al. “Energy-level scheme and transition probabilities of Cl-like ions”. In: *Atomic Data and Nuclear Data Tables* 28 (1983), pp. 355 – 377.

[127] E. Landi et al. “CHIANTI – an atomic database for emission lines”. In: *Astronomy and Astrophysics Supplement Series* 135 (1999), pp. 339–346.

[128] G. Del Zanna et al. “CHIANTI - An atomic database for emission lines. Version 8”. In: *Astronomy & Astrophysics* 582, A56 (2015), A56.

[129] E. Träbert. “Experimental checks on calculations for Cl-, S- and P-like ions of the iron group elements”. In: *Journal of Physics B: Atomic, Molecular and Optical Physics* 29 (1996), pp. L217–L224.

[130] B. Fawcett. “Calculated wavelengths, oscillator strengths, and energy levels for allowed 3-3 transitions for ions in the Cl-like isoelectronic sequence between Ar II and Ni XII”. In: *Atomic Data and Nuclear Data Tables* 36 (1987), pp. 151 –166.

[131] B Saha and S Fritzsche. “M1 and E2 transitions in Ar II”. In: *Journal of Physics B: Atomic, Molecular and Optical Physics* 38 (2005), pp. 1161–1171.

[132] C. Z. Dong et al. “Branching ratios and lifetimes for the low-lying levels of Fe xx”. In: *Monthly Notices of the Royal Astronomical Society* 307 (1999), pp. 809–814.

[133] S. Fritzsche, C. DONG, and G. GAIGALAS. “Theoretical wavelengths and transition probabilities for the 3d9–3d84p AND 3d84s–3d84p Transition arrays in Ni II”. In: *Atomic Data and Nuclear Data Tables* 76 (2000), pp. 155 –175.

List of Figures

List of Tables

Publications

During this Ph.D. thesis, the author has contributed to the following publications:

- Ab initio calculations of energy levels, transition rates and lifetimes in Ni xii
  M. Bilal, R. Beerwerth, A. V. Volotka, S. Fritzsche
  Monthly Notices of the Royal Astronomical Society, 469, 4620 (2017).
  https://doi.org/10.1093/mnras/stx1203
- Line strengths of QED-sensitive forbidden transitions in B-, Al-, F- and Cl-like ions
  M. Bilal, A. V. Volotka, R. Beerwerth, S. Fritzsche
  Physical Review A, 97, 052506 (2018).
  https://doi.org/10.1103/PhysRevA.97.052506
- Lifetime measurements of ultra-short-lived excited states in Be-like ions
  J. Rothhardt, **M. Bilal**, R. Beerwerth, A. V. Volotka, V. Hilbert, Th. Stöhlker, S. Fritzsche and J. Limpert
  X-Ray Spectrometry, Special Issue, page 1-4, (2019).
  https://doi.org/10.1002/xrs.3079
- High precision calculations of the $1s^2 2s2p\ ^1P_1 - 1s^2 2s^2\ ^1S_0$ spin allowed $E1$ transition in C III
  M. Bilal, A. V. Volotka, R. Beerwerth, J. Rothhardt, V. Hilbert and S. Fritzsche
  Physical Review A, 99, 062511 (2019)
  https://10.1103/PhysRevA.99.062511
- QED radiative corrections to the $^2P_{1/2}$ - $^2P_{3/2}$ fine-structure in fluorinelike ions
  A. V. Volotka, **M. Bilal**, R. Beerwerth, X. Ma, Th. Stöhlker, and S. Fritzsche
  Physical Review A, 100, 010502(R) (2019)
  https://10.1103/PhysRevA.100.010502

Ehrenwörtliche Erklärung

Ich erkläre hiermit ehrenwörtlich, dass ich die vorliegende Arbeit selbstständig, ohne unzulässige Hilfe Dritter und ohne Benutzung anderer als der angegebenen Hilfsmittel und Literatur angefertigt habe. Die aus anderen Quellen direkt oder indirekt übernommenen Daten und Konzepte sind unter Angabe der Quelle gekennzeichnet.

Bei der Auswahl und Auswertung folgenden Materials haben mir die nachstehend aufgeführten Personen in der jeweils beschriebenen Weise unentgeltlich geholfen: Prof. Dr. Stephan Fritzsche und Dr. Andrey V. Volotka.

Weitere Personen waren an der inhaltlich-materiellen Erstellung der vorliegenden Arbeit nicht beteiligt. Insbesondere habe ich hierfür nicht die entgeltliche Hilfe von Vermittlungs- bzw. Beratungsdiensten (Promotionsberater oder andere Personen) in Anspruch genommen. Niemand hat von mir unmittelbar oder mittelbar geld-werte Leistungen für Arbeiten erhalten, die im Zusammenhang mit dem Inhalt der vorgelegten Dissertation stehen.

Die Arbeit wurde bisher weder im In- noch im Ausland in gleicher oder ähnlicher Form einer anderen Prüfungsbehörde vorgelegt.

Die geltende Promotionsordnung der Physikalisch-Astronomischen Fakultät ist mir bekannt.

Ich versichere ehrenwörtlich, dass ich nach bestem Wissen die reine Wahrheit gesagt und nichts verschwiegen habe.

Jena, den

....
Moazzam Bilal

Curriculum Vitae

Personal Information

Name	Moazzam Bilal
Gender	Male
Nationality	Pakistani
Date of birth	28.08.1981
Place of birth	Gujranwala, Pakistan
Marital status	Married

School education

1987 – 1992	Govt. Primary School Dahaunkal, Gujranwala, Pakistan
1992 – 1995	Punjab Model High School Wazirabab, Pakistan
1995 – 1997	Govt. Model High School Kasur, Pakistan
1997 – 2000	Govt. FC College Lahore, Pakistan

University education

2000 – 2003	Bachelor in Physics, Government Islamia College Civil Lines, University of the Punjab, Lahore, Pakistan
2003 – 2006	Master in Physics, Department of Physics, University of the Punjab, Lahore, Pakistan
2007 – 2008	M.Phil in Physics, Pakistan Institute of Engineering and Applied Sciences, Islamabad, Pakistan

Employment

2009 – 2015	Research fellow in Department of Physics and Applied Mathematics, Pakistan Institute of Engineering and Applied Sciences, Islamabad, Pakistan
2016 – 2019	PhD scholar in Helmholtz Institute Jena, Friedrich Schiller University Jena, Germany under DAAD / HEC-Pakistan scholarship program

Jena, den ....

Moazzam Bilal